uc3m | Universidad Carlos III de Madrid

Bachelor Degree in Aerospace Engineering

2018-2019

Bachelor Thesis

"Study of the inertia effects on the auto-rotation of a samara seed"

Fernando Aspás Venegas

Supervisor

Gonzalo Arranz Fernández

Leganés, 2019

ABSTRACT

Autorotation motion which is exhibited by samara seed constitutes a marvellous and complex problem. Samara seeds, after a transient, enter in a sustainable steady rotational motion while reducing its descent speed. Problem complexity relies on coupling mechanisms behind autorotation; a subtle coupling between inertia and aerodynamic is responsible for this peculiar motion.

Autorotation has been studied for several decades and recently using the more advanced mathematical tools as DNS simulations, trying to assess autorotation. Nevertheless, nobody has tried before analyzing inertia effects on the autorotation. This thesis aims to understand the contribution of inertia effect by means of a numerical model based on the Blade Element Method. Two parametric studies are performed to provide insight into inertia effects. In order to do so, samara inertia properties were altered by, first, displacing the Leading Edge Rod and, secondly, changing seed mass distribution. The aerodynamic module was preserved across both studies by conserving the same original wing and weight force by keeping constant seed's mass.

General trends of variables of motion have been provided as inertia properties were altered. It was confirmed that both inertia properties, as well as seed's center, contribute to stability. Unstable frontier was found to be closed to the one proposed by Norberg. Moreover, the angle of principal direction has shown to be important suggesting a possible coupling on both directions (spanwise and chordal directions). Furthermore, optimal values of autorotation were found for similar values of the angle of principal direction in both studies presented in the thesis.

Key words: Research; Autorotation; Inertia; Aerodynamics; Coupling; Samara; Seed; Leading Edge; Leading Edge Rod; Blade Element Method; Parametric studies.

ACKNOWLEDGEMENTS

Life itself might be considered a coupling problem. Everything that occurs depends on yourself and your environment. For that reason, I must acknowledge the direct and indirect contributions that I have received for the development of this thesis, as well as during my bachelor studies.

First, I would like to thank professor Oscar Flores for the opportunity given in the thesis and all the help received. Also, thank you to my supervisor Gonzalo, who had helped and guided me through the development of the thesis. Without you, I would not have been able to complete such a thesis. You have been incredibly patient and helpful in any related topics. Moreover, you have transmitted a great amount of knowledge and your research interest over the topic.

I would like to express my gratitude to all my classmates and friends of UC3M, especially to Pablo Alejandro, Pablo Turégano and Natalia. I cannot remember any good moment in which any of you were present. These five years you have seen me in any possible situation and you have proven yourself to be ones of my closest friends. Although the future may temporarily separate us, I am certainly sure it will not change anything.

Thanks to my friends of Jaén, Torremolinos and Bristol, I would not certainly be the person that I am today without your contributions.

I want to thank my friend Maria for her unconditional support. You have been the best friend that I could ask for. Although distance separated us, and even more in the future, I will be always a phone call away, any time.

Most importantly, I want to express my most and deep gratitude to my family and dedicate this thesis to them, you are the ones that made this possible. Thank you for providing me with the opportunities that I am having in my formation, I know the effort that entails. Thank you for your infinite teaching and support, each one in a different way. Moreover, thank you for sharing my achievements and encouraging me to pursue my goals. I hope to continue making you proud.

Moreover I would like to acknowledge also my aunt Elo for its contribution, you have been an infinite source of affection, love and teachings while I was growing and until now. I hope it will never end.

Lastly, this thesis is especially dedicated to my grandmother Maria. I hope my achievements would still make you proud if you could see me now.

CONTENTS

LIST OF FIGURES

LIST OF TABLES

NOMENCLATURE

Acronyms

BEM Blade Element Method

BET Blade Element Theory

DNS Digital Numerical Simulation

DOF Degree Of Freedom

LCM Local Circulation Method

LE Leading Edge

LER Leading Edge Rod

LEV Leading Edge Vortex

MAV Micro Air Vehicle

PIV Particle Image Velocimetry

RPA Remotely Piloted Aircraft

Symbols

α Effective angle of attack

β Coning Angle

$\boldsymbol{q}$ Quaternion vector

$\boldsymbol{u}_G$ Velocity of seed's gravity centre

$\boldsymbol{x}_G$ Position of seed's gravity centre

$\boldsymbol{x}_{ICR}$ Position of Instantaneous Center of Rotation

λ $= \Omega r_t / w_d$, tip speed ratio

ν Viscosity of fluid

ϕ Spinning Angle

ψ Precession Angle

ψ' Precession Angle (Euler)

ρ_f Density of the fluid

ρ_s Density of the seed

θ Coning angle

θ' Nutation Angle

ϱ $= \rho_s / rho_f$, density ratio

b Wing Span of seed

c Maximum wing chord of seed

D_{LER} Diameter of Leading Edge Rod

g Gravity acceleration

h_n Seed's nut semiminor axis

L_{LER} Length of Leading Edge Rod

R $= y^*/b$, Ratio of position of maximum chord

r_n Seed's nut semimajor axis

r_t Distance from the gravity centre to the wing tip

Re Reynolds number

S Samara's wing surface

t_w Wing thickness of seed

V_s Volume of seed

w_d Descent speed

W_s Samara's weight

x_{LER}, y_{LER} Position of Leading Edge Rod

Superscripts

$\boldsymbol{x}^B$ Vector x expressed in $\sum_B$

$\boldsymbol{x}^C$ Vector x expressed in $\sum_C$

$\boldsymbol{x}^L$ Vector x expressed in $\sum_L$

$\boldsymbol{x}^P$ Vector x expressed in $\sum_P$

1. INTRODUCTION

In this chapter, an overview of the present research project is presented. Main motivation to derive this thesis is outlined in section 1.1. State of the art related to samara seeds with the available literature is introduced in section 1.2, together with the main engineering applications that author found or proposed, section 1.3. The socio-economic and legal framework of proposed engineering applications is analysed in section 1.4.

The objectives of the thesis are gathered in section 1.5, while the thesis structure is outlined in section 1.6.

1.1. Motivation

Nature has always been a research and point of interest of the scientific world. Everything in nature is designed by billions of years of evolution by which each element has tended to be optimal to their environment, while the less adapted are eliminated in the process. This common-known try-error process is applicable to any aspect. Therefore, it is not surprising that current seeds accomplish their functionality perfectly, that is to disperse successfully. Many of them take advantage of the wind to successfully spread, with different used techniques with a dispersal potential ranging from meters to kilometers (Nathan, 2006). Some of these seeds disperse themselves taking advantage of viscous forces such as dust seeds and spores (floaters) (Augspurger, 1986). Others such as plumed seeds move at higher Reynolds numbers working as real parachutes in which drag force is predominant (Burrows, 1975). However, there are other kinds of seeds, of interest here, that generate actively lift force, therefore, reducing their falling rate and increasing dispersal by lateral winds. This type of seeds, usually known as winged-seeds or samaras, generates aerodynamic forces by a sustainable autorotation motion (Azuma, 2006).

Samaras exhibit different sizes and shapes, but all of them have similar physical structure. From a macroscopic point of view, a winged seed can be mainly decomposed in: a thin wing reinforced with ribs providing bending stiffness, a relative thick leading edge and an embryo nut at one side of the wing. Multiple samara seeds are displayed in 1.1a.

Winged seeds have an inherent ability to entrance in autorotation, no matter the initial conditions in which seed is released. This process is described by Norberg (1973). Furthermore, they exhibit high stability motion to external perturbations as wind disturbance, but also to change in the geometrical shape (see Varshney et al. (2011)). In this fashion, samaras possess self-stability governed just by their structural pattern, without the need of any active actuator, like neuromuscular control in animal flight (Norberg, 1973).

Autorotation motion consists of a subtle couple between inertia properties and aerodynamics. The theoretical complexity lays on this coupling. A seed falling at a certain

(a) (b)

Fig. 1.1. (a) View of multiple samara seeds of Acer palmatum (taken from stapeliagarden.blogspot.com). (b) Autorotational flight of a maple seed at different time instants (Lentink et al., 2009)

descent speed, angular velocity, and attitude depend on the aerodynamic forces, which in turn, will depend again on the former ones. The aerodynamic model of the thesis is built based on this dependency on kinematics.

The study of this particular motion has always been an object of study according to the available bibliography. However, studies were mainly based on the development of momentum theory and experimental data. Most recently, as technology develops, samaras were again in the focus of study. Lentink et al. (2009), with the aid of Particle Image Velocimetry (PIV), observed the stable Leading Edge Vortex generated on the upper wing surface, linking to the high lift performance attained by samara when autorotation. Moreover, most interests were raised regarding the development of Micro Air Vehicles (MAVs) based on samara shapes.

There are many reasons to study again this elegant coupled motion. Although most recently authors as Lee (2016) and Arranz et al. (2018a) developed more accurate numerical based on Direct Numerical Simulations (DNS), nobody has -at least to author's knowledge- made a study on the effect of inertia properties on autorotation, although it was proposed before (Roccia et al., 2014; Arranz et al., 2018a). Some authors as Varshney et al. (2011), explained angular momentum equation evolution during transient leading to autorotation. While other as Ulrich et al. (2010) analysed the different motions modes available in their designed MAV.

Analysing inertia properties effect on autorotation can be a difficult problem. First of all, imposing inertia properties might produce irregularities when solving the inverse problem (obtain the geometry from given inertia properties) such as: unrealistic geometric configurations, multiple geometries or no solution at all. Therefore, the procedure will be based on parametric studies of multiple simulations in which some parameters of seed are

changed oaintaining constant the aerodynamic module. Nevertheless, DNS simulations are quite expensive. They require a large amount of computational time, for example, days of computational time, which will not serve for a parametric study. Therefore, a simplistic tool is developed so quicker computational simulations are reached in order to understand autorotation trends as inertia is varied.

Therefore, interested in the nature of the problem, the absence of research regarding inertia properties and the huge contribution over the autorotation motion. Author develops a simplistic model based on Blade Element Method (BEM) in order to perform parametric studies of the inertia properties of samaras seeds.

1.2. State of art

Autorotation of samara is a topic that has been studied for several years and by several authors. Reader must regress to find the first scientific and complete study of a single-winged samara (Norberg, 1973). Norberg (1973) employed the simple momentum theory to explain the dynamics of a samara in autorotation, especially focusing on pitch stability and concluding that seed stability is based on the uneven seed mass distribution.

Moreover, Green (1980) measured experimentally the rate of descent, angular velocity, orientation and other parameters of different seed species using strobe photographs. The experimental data was used to conclude the direct proportionality of descent velocity with wing loading.

Augspurger (1986) continued the same investigation line presenting multiple linear regressions for each specie, considering seeds with different dispersal techniques as dust and spores. He related the wing loading with rate of descent as Green (1980) previously. He found agreement with momentum theory, the descent velocity increases as wing loading does the same.

The first computational study contrasted with empirical data is introduced by Azuma and Yasuda (1989), who applied Local Circulation Method (LCM), described in Azuma (1981) to estimate the forces distribution on a Maple seed. In order to do so, wing is discretized in chordwise sections in which forces are computed approximating each section as two-dimensional aerofoil, similarly to BEM. Velocities and attitude of seed were imposed assuming momentum conservation in the vertical direction and equilibrium of moments, together with further simplifications. In the same line, Roccia et al. (2014) developed an Unsteady Vortex-Lattice Method to study samara autorotation aerodynamics while their kinematics is based on flight parameters of real samaras.

Other modern mathematical study models were developed at Seter and Rosen (1992b,a). First, Seter and Rosen (1992b) developed a numerical model based on Blade Element Method to compute the aerodynamics while using the six degrees of freedom equations of motions simplified under steady autorotative conditions: constant vertical and angular velocity. Moreover, Seter and Rosen (1992a) address stability of samara in autorotation

based on the equation of motion previously presented in their preceding paper. They concluded remarking the good correlation with experimental data and the importance of the uneven chordwise distribution of mass by means of parametric studies similar to the ones presented in the current thesis. Nevertheless, the inertia effect on autorotation are not analysed.

Entrance into autorotation from rest has been treated by Yasuda and Azuma (1997) as well as Norberg (1973) previously. Yasuda and Azuma (1997) tested experimentally with stroboscope photography and a wind tunnel: different flat plane wings, real samaras, modified ones and artificials built samaras. They finally conclude that for the autorotational flight of samaras in a plane configuration, the most important factors guaranteeing the low rate of fall are the airfoil camber and the surface roughness, including the thickness near the leading edge of the wing. To enter into a stable autorotation the mean camber line must be downwardly convex at least near the wing root or near the center of gravity location. The surface roughness is necessary to improve the aerodynamic characteristics of the airfoil for the flight at low Reynolds number so as to increase the driving torque about the autorotational or spin axis. This torque is obtained by the forward inclination of the aerodynamic lift and is large enough to oppose the resisting torque generated by the aerodynamic drag (Azuma, 1981; Azuma and Yasuda, 1989). In contrast to the above airfoil characteristics, the platform of the wing was found less influential on the autorotational flight (Yasuda and Azuma, 1997).

Further analysis of modification of real samaras was presented by Varshney et al. (2011). Varshney *et al.* measured experimentally with high-speed digital cameras the kinematics of a samara subjected to different conditions. They explained unsteady transition from rest until autorotation, as well as performing experimental cuts to samara concluding that only when the nut is completely removed, the seed no longer gyrates and falls erratically (Varshney et al., 2011).

Using DPIV, Lentink et al. (2009) identified the formation of the LEV in the upper surface of an Acer Maple seed as it spins. Moreover, LEV is responsible of the high-performance lift attained by samara and wing insects at high angles of attack and low values of Re. LEV remains compact and attached due to large spanwise flow (Birch and Dickinson, 2001).

Rao et al. (2014) developed a numerical model based on BEM similar to the one developed in the current thesis discussing the flow regimes: turbulent and windmill that can be observed in mahogany seeds in autorotation.

Most recently, DNS method has been implemented to simulate samara autorotation Lee (2016); Arranz et al. (2018b) and extracted more results about autorotation, agreeing with LEV theory and previous analysis.

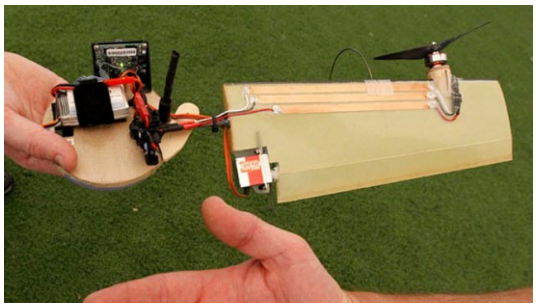

(a)

(b)

Fig. 1.2. (a) Lockheed Samarai-MAV prototype (source: technovelgy.com) . (b) Ulrich MAV prototype (Ulrich et al., 2010)

1.3. Engineering Applications

One may think that the high aerodynamic efficiency, as well as the autorotative motion attained by samara seed, can inspire artificial aerial vehicles. In fact, many scientists and even industry, have developed vehicles based on samara shapes that exploit this phenomenon, especially last decade with the technology development of the commonly known *drones* or Remotely Piloted Aircraft (RPA). Moreover, the engineering applications not only amount to be used as RPA but also the development of vehicles that could benefit from autorotation passively to reduce their descent speed.

At this point, vehicles based on samara seeds can be categorised under two main divisions: powered and non-powered vehicles. While the first one benefits from samara shapes to induce rotation by means of actuators as propellers, that provide thrust and that hopefully will lead to controllability. The non-powered vehicles will use samara autorotative properties passively with dispersal purposes. Due to these differences, both types of samara shaped vehicles will have different applicability. Reader should be remarked that when referring to these kinds of small vehicle, acronym Micro Air Vehicle (MAV) is commonly used.

On one hand, powered samara vehicles might lead to the development of RPAs based on this peculiar shape. Companies as Lockheed Martin have already developed one based on these seeds around 2010. Several studies were openly published regarding the conceptual design of these MAVs (Jameson et al., 2007; Fregene et al., 2011; Jameson et al., 2012) until finally a prototype named Lockheed Samarai-MAV was built. Samarai-MAV presents similarity with real samaras as displayed in figure 1.2a. However, it is quite big around 0.4 m of span and with a weight of 0.5 kg. Moreover, another smaller prototype was studied and designed in 2010 (Ulrich et al., 2010). Ulrich et al. (2010) designed a nano-scale robotic monocopter samara displayed in figure 1.2b. Configuration of the prototype, displayed at figure 1.2b, is similar to Lockheed one. Nevertheless, Ulrich's wing displayed a clean wing attached to a motor in the primary structure that can modify the wing pitch angle in order to be controlled.

(a)

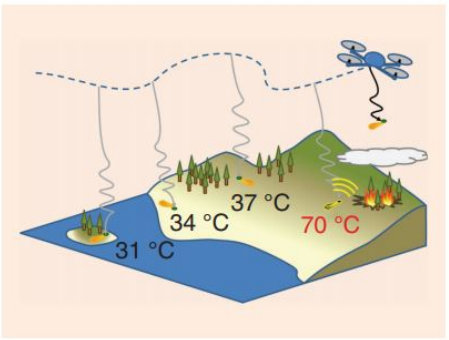

(b)

Fig. 1.3. (a) A prototype of samara with sensors (source: technovelgy.comrobotics.itee, Pounds and Singh (2015)). (b) Schematics of system operation as proposed by Pounds and Singh (2015)

Moreover, author suggests that understanding inertia effect on autorotation can provide some advantages on the development of these vehicles. Previous MAVs based their controllability on the movement of control surfaces, modifying their aerodynamics, as well as modifying the level thrust. Nevertheless, modification of inertia properties on flight by internal movement of mass might lead to RPA controllability as well, by modifying inertia properties on moment equations.

On the other hand, unpowered samaras exhibit quite a large number of applications. Firstly, artificial samaras with sensors can be used to benefit from dispersal capabilities. Samaras can be released from another vehicle at a height and, therefore a map of different properties of a region might be produced as samaras dispersed over the region of interest. The complexity of system and sensors onboard of these samaras will depend on the envisaged applications. For example, Pounds and Singh (2015) developed a network of artificial samaras-vehicles with sensors with the purpose of fire prevention. These samaras will possess temperature sensors that will emit a signal when, for example, the temperature exceeds some threshold value, indicating a possible source location of a fire. Nevertheless, applications are infinite: air cleanliness, amount of light...

Secondly, not only dispersal samara capabilities could be exploited, but autorotation as aerodynamic brake or parachute. Vehicles able to autorotate while falling might be designed to reduce descent speed to an intended value. This applicability branch could result in spacecraft design for entrance in a planet gravity field, reducing experienced acceleration by the generation of lift, and consequently landing on its surface successfully in a controlled way. This line of investigation was already investigated by NASA (Burke, 1989; Kroo, 1995).

1.4. Socio-economic and Legal framework

Benefits from applications of powered and unpowered samara vehicles become evident from previous section discussion. These vehicles might be designed envisaging different application to serve human beings. Nevertheless, as in any aspect of current society, the incursion of new technologies will results in a socio-economic impact, leading to the development of a legal framework under which these new technologies may operate, ensuring society safety.

Due to the number of applications, discussion in the section will be mainly focused on RPAs, which, although it is a new technology, it is already impacting in society as well as being one of the primary growing industries in the aerospace field. Moreover, regulations of drones have been put in place and had been renewed.

In economical importance, the drone industry is not minor. It is a young industry with very promising numbers. Only in the USA, there were around 1.25 million drones registered by the end of 2018 with a mass between 0.55 and 55 pounds, according to FAA. Unmanned Aerial Vehicles (UAV) will result in benefits in the USA of approximately 82,100 million dollars between 2015-2025, creating up to 103,000 jobs in the USA (Jenkins and Vasigh, 2013). Furthermore, Goldman Sachs estimated that drone technologies will reach a total market value of 100 billion between 2016-2020. However, the majority of market activity will be linked to military projects, while the commercial business will represent the quickest growing opportunities, with an estimated projection of 13 billion between these years.

In terms of the legal framework, although it is recent, some regulation has been put in place and has been renovated along the years. In particular in Spain, country of the author, regulations are dictated in royal decree 1036/2017 of 15th December 2017, which was published later in BOE publications (official gazette of the Kingdom of Spain).

It is important to remark that the project developed in the current thesis is based on the understanding of inertia effects on the autorotation of samara, with the final purpose of applying knowledge to develop applications, as for example MAVs based on these seeds. Therefore, no legal issues have been considered for the development of this research.

1.5. Objectives

As previously stated, the main objective of the thesis is the understanding of how inertia properties affect autorotation of a samara seed. This major objective already englobes several secondary objectives, as for example the development of the numerical model in order to perform the corresponding inertia study. Objectives are summarized as follows:

- To develop a reference geometry and inertia model of samara.
- To develop a numerical model to perform simulations.

- Validating the numerical model developed.
- To perform parametric studies of inertia properties.
- Post-processing results tasks. These are post-processing tasks associated to extract data from simulations, treating the data and representing the most relevant information intuitively.
- Analysis and interpretation of results from the parametric study.

It is important to remark that accomplishment of previous objectives, both primary and secondary, are directed towards a better understanding of autorotation that will result in applications for example in MAVs.

1.6. Thesis Structure

This project has been organized in four chapters and two appendices which are summarized below:

- Chapter 1 presents the motivation to develop this project. State of art summarizing bibliographic contributions along time is gathered. Existing samara-based vehicles, as well as possible applications of this geometry, are outlined. Additionally, the socio-economic and legal frameworks of these applications are briefly analysed. Finally, the main objectives to accomplish are outlined.
- Chapter 2 details the methodology followed to develop the accomplished project objectives. Equations used, samara model, aerodynamic model and numerical model are described.
- Chapter 3 gathers the results obtained, displaying validation and inertia parametric studies performed.
- Chapter 4 summarizes the conclusions extracted from the results.
- Appendix A contains the development of the inertia computations of the geometrical model.
- Appendix B details project planning followed together with an estimated budget.

2. METHODOLOGY

A samara is to be studied regarding the influence of inertia properties on its motion. The samara will be falling upon the effect of gravity through a fluid that will generate aerodynamic forces depending on position, velocity, and attitude. In order to fully understand this complex physical and mathematical problem, the problem is analysed developing a simple numerical model.

First of all, governing equations and different reference frames used are presented. For convenience, motion equations will be resolved in different reference frames, properly defined. Secondly, samara geometry is defined together with its associated inertia and mass distribution.

Then, an aerodynamic model is presented showing how aerodynamic forces are computed following BET, in which wing span is discretized in a given number of blades, where forces and moments will be computed independently and then blades contribution will conform the total samara aerodynamic force and moment.

Lastly, the numerical method developed is explained together with its relevant validation.

2.1. Governing equations

Samara is modeled as a rigid body, exhibiting 6 Degrees Of Freedom (DOF), so the dynamics are solved. Therefore, vectorial equations to be solved are Newton's second law together with angular momentum equation.

$$m_s \dot{\mathbf{u}}_G = \sum \mathbf{F} \tag{2.1}$$

$$\frac{d\mathbf{H}_G}{dt} = \sum \mathbf{M}_G \tag{2.2}$$

where in equation (2.1), m_s corresponds to the seed mass, $\boldsymbol{u_G}$ is the velocity of seed's gravity center while $\sum F$ are the external forces acting upon the seed. With respect to angular momentum equation (2.2), $\boldsymbol{H_G}$ is the angular momentum; $\sum \boldsymbol{M_G}$ is sum of external moments of the seed with respect to seed's gravity center.

In order to solve previous equations of motion (2.1) & (2.2), different reference frames need to be defined before, so equations are resolved accordingly. Relevant reference frames are defined in figure 2.1 .

First of all, an inertial reference frame $\sum_L$, called Laboratory, fixed at O and whose axis z_L will point downwards in the sense of the gravity, the other two axis $x_L y_L$ will complete the right hand rule in an horizontal plane. In addition, a body reference frame

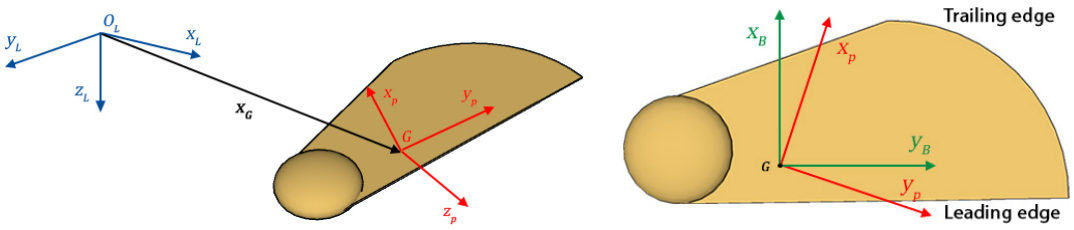

(a) (b)

Fig. 2.1. Sketch of the reference frame used: the inertial reference frame $\sum_L$, body attached principal axis of inertia $\sum_p$ and body reference frame $\sum_B$. Position vector $\boldsymbol{x}_G$ is also displayed.

$\sum_B$ was attached at samara's center of gravity and which axis y_B one will extend along the span (parallel to the Leading Edge) while x_B be directed in the chordal direction (from Leading Edge to Trailing edge). z_B will complete the right hand rule and it will initially point upwards. These both reference frames will be initially parallel, z_B will be directed in the opposite sense to z_L, x_B and x_L initially opposed, while y_B and y_L will be parallel. In conclusion, the initial difference of both reference frame will reside initially on a rotation of 180º around $y_L y_B$.

In addition to previous, there is still one important reference frame to be defined, principal axes of inertia $\sum_P$, it consists of another body attached reference frame centered again at the center of gravity, but this one will be directed in the principal directions of inertia, quite important in the dynamical analysis of the present thesis as entails a higher simplification of angular momentum equation (2.2).

One common choice to represent samara attitude will be the used of the very known Euler Angles $\psi'\beta'\phi'$, representing the consecutive relations that relate both the inertia reference frame $\sum_L$ and a body reference frame, $\sum_P$. Details covering the construction of the rotation matrix from Euler angles can be found in Ginsberg (2008); Tewari (2007). However, there are multiple choices of Euler angles that will yield the same resultant rotation between both axes, which is problematic. These singularities of body attitude can be overcome with the use of quaternions formulation to describe samara orientation Tewari (2007). Quaternions vectors are composed of four-term, the first three representing the direction of the rotation axis $\vec{e}$ while the fourth is related to the rotation angle φ.

$$q_i = e_i \sin\left(\frac{\varphi}{2}\right) \quad (i = 1, 2, 3), \quad \text{and} \quad q_4 = \cos\left(\frac{\varphi}{2}\right) \tag{2.3}$$

Time derivatives of $\boldsymbol{q}$ yields to be (Tewari, 2007):

$$\frac{d\mathbf{q}}{dt} = \frac{1}{2}\overline{\overline{Q}}\mathbf{q} \tag{2.4}$$

where $\overline{\overline{Q}}$ is a skew-symmetric matrix which depends on the angular velocity of the body

$\mathbf{\Omega}^P = (p, q, r)$ expressed in principal axis of inertia $\sum_p$.

$$\overline{\overline{Q}} = \begin{pmatrix} 0 & r & -q & p \\ -r & 0 & p & q \\ q & -p & 0 & r \\ -p & -q & -r & 0 \end{pmatrix} \tag{2.5}$$

Finally position evolution is given by

$$\frac{d\mathbf{x}_G}{dt} = \mathbf{u}_G \tag{2.6}$$

It is important to make some clarifications of previous equations (2.1)-(2.2). External forces applied on a samara comprises: gravity force ($\boldsymbol{F_g} = m_s g \boldsymbol{k_L}$), buoyancy force ($\boldsymbol{F_b} = -\rho_f V_s g \boldsymbol{k_L}$) and aerodynamic forces (F_A^B), which are computed in the body reference frame. However, it is more understandable to resolve second Newton's law in $\sum_L$ in order to, therefore, compute the seed position with respect to to this inertial reference frame. Furthermore, gravity and buoyancy forces are already expressed with respect to this frame. But aerodynamic forces are changed from $\sum_B$ to $\sum_L$, resulting in $F_A^L = (F_{A_x}^L, F_{A_y}^L, F_{A_z}^L)$. Thus, equation (2.1) turns to be:

$$m_s \dot{u}_G = F_{A_x}^L \tag{2.7}$$
$$m_s \dot{v}_G = F_{A_y}^L \tag{2.8}$$
$$m_s \dot{w}_G = F_{A_z}^L - m_s g + \rho_f V_s g \tag{2.9}$$

In equations (2.7)-(2.9), $\boldsymbol{u_G}^L = (u_G, v_G, w_G)$ corresponds to the velocity of the samara's center of gravity and V_s the volume of the fluid occupied by seed.

Regarding the moments, the only force that produces torque is the aerodynamic force as the point of the application of the rest of the forces is the seed's gravity center. Therefore $\sum \boldsymbol{M_G} = \boldsymbol{M_A}$. This equation is solved in $\sum_P$, and the moments are taken with respect to seed's gravity center as the development of $\frac{\partial \boldsymbol{H_G}}{\partial t}$ is largely simplified. Thus, the angular momentum equation results in

$$I_{p,x}\dot{p} - \left(I_{p,y} - I_{p,z}\right) qr = M_{A_x}^P \tag{2.10}$$
$$I_{p,y}\dot{q} - \left(I_{p,z} - I_{p,x}\right) rp = M_{A_y}^P \tag{2.11}$$
$$I_{p,z}\dot{r} - \left(I_{p,x} - I_{p,y}\right) pq = M_{A_z}^P \tag{2.12}$$

where I_p corresponds to the seed moments of inertia with respect to principal axis of inertia (principal moments of inertia and angular velocity $\Omega = (p, q, r)$ expressed in $\sum_P$

With previous equations (2.4),(2.6) and (2.7)-(2.12), all variables defining the dynamical system are defined. First, (2.7)-(2.9) will provide the evolution of velocity , $\frac{du_G}{dt}$,

(a) (b)

Fig. 2.2. Image of geometrical model compared with real Acer Maple samara on which model is greatly inspired. Real samara figure seed was taken from botanicayjardines.com

then (2.6) will provide the evolution of the position. Similarly, for the angular momentum, equations (2.10) - (2.12) will provide the derivative of the angular momentum and therefore the evolution of the angular velocity Ω and, consequently, attitude evolution by (2.4).

2.2. Samara model

During this section, the samara model employed in simulations is presented. In addition to the geometrical configuration of samara, samara properties relevant to motion as inertia properties, of vital importance in this thesis, are presented in detail.

2.2.1. Geometry

Real samara seeds exhibit quite complex geometries. They have an elastic wing reinforced by ribs and fibers that extend from the relatively thick leading edge in the chordal direction. Moreover, the wing is bent and twisted exhibiting concavity, essential for the entrance in autorotation from rest (Norberg, 1973; Yasuda and Azuma, 1997). Thus, seed size complicates taking measurements, usual samaras posses maximum chords in the interval $[2-3]cm$ (Azuma and Yasuda, 1989; Yasuda and Azuma, 1997). Therefore due to these geometries issues, it becomes evident the need for an alternative simplified model. Moreover the simplification allows parametric study by means of key geometric parameters.

When referring to autorotation seeds, which rotates while falling reducing their descent speed, different samara species can be found, with different geometries (i.e. different span, chord distribution, thickness...) (Augspurger, 1986; Yasuda and Azuma, 1997). The simplified model developed geometrical contour is based on Acer Maple's seeds.

Model, displayed in figure 2.2, is composed mainly of three elements

- Nut is modeled as an oblate spheroid

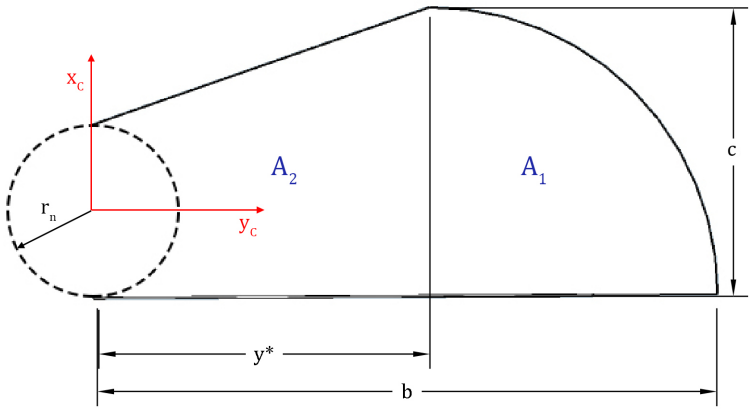

Fig. 2.3. Sketch of wing platform showing their geometrical parameters that seize it, together with the respective areas definition and $\sum_C$ auxiliary reference frame used for computations

- Wing is modeled as a thin flat surface, built as the sum of an outer tip quarter of a circle (A_1) and a trapezium surface (A_2), as displayed in fig. 2.3.
- Leading Edge Rod (LER) which is modeled as a narrow cylinder that expands along the span direction up to 80% of span length. The length was limited so that when LER is displaced when analysing results, it will not expand out of the wing surface as in real winged-seeds.

This artificial leading edge, modeled as a cylinder, is of great importance, as seen in results. The uneven mass distribution of the leading edge together with wing concavity seems to be responsible for seed stability, especially in pitch, according to bibliographic research (Norberg, 1973; Yasuda and Azuma, 1997; Seter and Rosen, 1992a; Ulrich et al., 2010). Furthermore, Seter and Rosen (1992a) showed in their parametrization study the importance of the leading edge encharged not only of moving forward the seed's gravity center but of modifying the inertia properties, so stability is enhanced. Moreover, according to them, as Leading Edge Rod mass is continuously increased, there will be a point from which instability behaviour will occur. This will be latter checked in results section.

Figure 2.3 displays the wing platform identifying the geometrical key parameters, that fully constraint the geometry: r_n corresponds to the nut radius (semimajor axis); h_n/r_n named oblateness ration which is the ratio of h_n, semiminor axis, and r_n, semimajor axis; b is the wingspan, defined as the distance from the center of the nut; c corresponds to the maximum chord located at y^* given by $R = y^*/b$. Furthermore the parameters left to be defined are the ones related to Leading Edge Rod: D_{LER} Leading Edge Rod diameter; L_{LER} which is its length; and rod centroid (x_{LER}, y_{LER}). Using $\sum_C$ ref. frame, vector position of LER is $\boldsymbol{x}^C_{LER} = x_{LER}\,\boldsymbol{i}_c + y_{LER}\,\boldsymbol{j}_c$.

It is important to notice that wing span will be given as by equation (2.13) due to compatibility between trapezium and quarter of circle areas at the point of the maximum

chord.

$$b = \frac{c}{1 - R} \tag{2.13}$$

Resulting as $b = 2.1739c$ for the nominal geometry described in this section.

r_n	h_n/r_n	R	t_w	D_{LER}	L_{LER}	x_{LER}	y_{LER}
0.3c	0.44	0.54	0.0035c	0.03c	0.8b	$-r_n$	0.4b

In addition to the previous parameters, there are still variables not affecting winged-seed platform but mass and inertia properties. These are the density properties both of the seed, ρ_s and the one of the LER, ρ_{LER}. It was taken $\frac{\rho_s}{\rho_f} = 300$ as an estimation of density ratio of real samaras that, according to literature, range in the interval $\frac{\rho_s}{\rho_f} \approx [100 - 1000]$. For the LER, $\frac{\rho_{LER}}{\rho_s} = 4$ so that contribution of LER is enhanced in motion when varying it in the results section. Moreover, according to Norberg (1973), contribution of leading edge must be enough so seed's center of gravity lies between 25-30% of the chord, behind the LE. So D_{LER} together with ρ_{LER} were chosen accordingly satisfying logical geometrical constraints. Norberg also relates the position of seed's center of gravity to pitch stability and the resultant autorotation steady state. The farther back the C.G. larger angle of attack and steeper the glide path.

2.2.2. Inertia properties

Equations regarding the angular momentum (2.10)-(2.12) are expressed in principal axes of inertia. Therefore principal inertia must be known together with their associated directions, giving the orientation of principal axis as well as seed center of gravity providing origin of reference frame.

Center of gravity

First, seed's center of gravity is computed in order to provide the locus for the different reference frames depicted in section 2.1. For this purpose, geometry is decomposed in several pieces. Wing is subdivided in mass 1 (quarter of circle, A_1) and mass 2 (trapezium, A_2) while nut and LER will maintain their own names.

$$m_1 = \rho_s t_w \frac{\pi c^2}{4} \tag{2.14}$$

$$m_2 = \rho_s t_w \left(\frac{(2r_n + c)y^*}{2} - \frac{\pi r_n^2}{2} \right) \tag{2.15}$$

$$m_n = \rho_s \frac{4}{3} \pi r_n^2 h_n \tag{2.16}$$

$$m_{LER} = \rho_{LER} \frac{\pi D^2}{4} L_{LE} \tag{2.17}$$

Mass 2 computations are more complex than the others due to the geometrical definition, it was computed by subdividing it into 2 other surfaces: "trapezium" and a half semicircle. Therefore, the resulting area of interest corresponds to the trapezium subtracting half the circle (half of the nut platform).

Centroids of each area are commonly known by geometric and symmetry principles (Ginsberg, 2008) as

- $\boldsymbol{r}^{\boldsymbol{C}}_{\boldsymbol{G,w1}} = (r_n - \frac{4c}{3\pi}, y^* + \frac{4c}{3\pi}, 0)$
- $\boldsymbol{r}^{\boldsymbol{C}}_{\boldsymbol{G,n}} = (0, 0, 0)$

However wing area 2 centroid is not directly obtained and entails higher mathematical development. As centroid of the trapezium is not readily obtainable, the trapezium is decomposed in a rectangle triangle and a rectangle whose centroids are commonly known. Therefore A2 centroid is computed by its definition $\boldsymbol{r} = \frac{\sum r(i)A(i)}{\sum A(i)}$ by substracting semicircle contribution as

$$\boldsymbol{r}^{\boldsymbol{C}}_{\boldsymbol{G,w2}} = \frac{A_{triangle}\boldsymbol{r}^{\boldsymbol{C}}_{\boldsymbol{triangle}} + A_{rectangle}\boldsymbol{r}^{\boldsymbol{C}}_{\boldsymbol{rectangle}} - A_{semicircle}\boldsymbol{r}^{\boldsymbol{C}}_{\boldsymbol{semicircle}}}{A_{triangle} + A_{rectangle} - A_{semicircle}} \tag{2.18}$$

where the denominator just consist on the wing area 2.

Then seed's center of gravity is computed as

$$\overline{\mathbf{r}}^{C}_{G} = \frac{\overline{m}_{w1}\mathbf{r}^{C}_{G,w1} + \overline{m}_{w2}\mathbf{r}^{C}_{G,w2} + \overline{m}_{n}\mathbf{r}^{C}_{G,n} + \overline{m}_{LE}\mathbf{r}^{C}_{G,LE}}{\overline{m}_{s}} \tag{2.19}$$

where masses are non-dimensionalized with $\rho_s c^3$, as $\overline{m} = \frac{m}{\rho_s c^3}$. For the nominal case resulting values are summarized in table 2.1

$\overline{m}_{w1}$	$\overline{m}_{w2}$	$\overline{m}_{n}$	$\overline{m}_{LER}$	$\overline{m}_{s}$
0.0027	0.0028	0.0498	0.0061	0.0615

Table 2.1. Non-dimensional masses of the seed different parts together with the seed's mass

So center of gravity is located at $\overline{\mathbf{r}}^{C}_{G} = (-0.0186, 0.1915, 0)$ according to equation (2.19) Therefore origin of $\sum_P$ and $\sum_B$ are located.

Inertia

Due to chosen geometry, inertia calculations are quite extensive and does not provide any insight for this thesis development. Therefore they are not presented in this section, the reader is referred to appendix A. Instead computational steps are outlined below together with the final inertia properties.

Nut inertia properties with respect $\sum_C$ are easily obtained from Ginsberg (2008) as

$$I^C_{x_{nut}} = \frac{1}{5}m_n(r_n^2 + h_n^2) \qquad I^C_{y_{nut}} = \frac{1}{5}m_n(r_n^2 + h_n^2) \qquad I^C_{z_{nut}} = \frac{2}{5}m_n r_n^2 \tag{2.20}$$

Nut properties are easily displaced to seed's gravity center using *Steiner's theorem*.

For the wing, again the wing is divided into two mains parts: an outer quarter circle and a trapezium. The quarter circle is easily obtained by bibliographic research. Yet, it was computed by performing the corresponding integration with respect to its center, $\overline{\overline{I}}^{O_{quarter}}_{Area1}$. Then translated to its center of mass using *Steiner's* $\overline{\overline{I}}^{c_{quarter}}_{Area1}$ and again using *Steiner's* in order to be translated to the point of interest, seed's center of gravity $\overline{\overline{I}}^{C}_{Area1}$ .For Area 2 process is more complicated. As this volume is subdivided into other two, whose contributions are summed or subtracted when they are taken with respect to the seed's gravity center. Computational steps are summarised just below:

1. The inertia of each part is computed at once by performing the corresponding integrals over the whole volume, resulting in $\overline{\overline{I}}^{C}_{trap}$ and $\overline{\overline{I}}^{C}_{semic}$, which are the inertia of trapezium and semicircle, respectively. In order to know the inertia of Area 2 wing with respect to $\sum_C$, it will just be the one of the trapezium subtracting the one of semicircle. But inertia properties are required to be known at the seed's gravity center, so each inertia must be translated independently.

2. Inertia is calculated at each centroid respectively, using *Steiner's theorem*.

$$\overline{\overline{I}}^{c_{trap}}_{trap} = \overline{\overline{I}}^{C}_{trap} - m_{trap}\left(r^2_{OCc_{trap}}\overline{\overline{U}} - \left[\boldsymbol{r}_{\boldsymbol{OCc_{trap}}}\boldsymbol{r}_{\boldsymbol{OCc_{trap}}}\right]\right) \tag{2.21}$$

$$\overline{\overline{I}}^{c_{semic}}_{semic} = \overline{\overline{I}}^{C}_{semic} - m_{semic}\left(r^2_{OCc_{semic}}\overline{\overline{U}} - [\boldsymbol{r}_{\boldsymbol{OCc_{semic}}}\boldsymbol{r}_{\boldsymbol{OCc_{semic}}}]\right) \tag{2.22}$$

3. Inertia is translated to the final point, samara's center of gravity applying once again *Steiner's theorem*

$$\overline{\overline{I}}^{B}_{trap} = \overline{\overline{I}}^{c_{trap}}_{trap} + m_{trap}\left(r^2_{OBc_{trap}}\overline{\overline{U}} - \left[\boldsymbol{r}_{\boldsymbol{OCc_{trap}}}\boldsymbol{r}_{\boldsymbol{OCc_{trap}}}\right]\right) \tag{2.23}$$

$$\overline{\overline{I}}^{B}_{semic} = \overline{\overline{I}}^{C}_{semic} + m_{semic}\left(r^2_{OBc_{semic}}\overline{\overline{U}} - [\boldsymbol{r}_{\boldsymbol{OBc_{semic}}}\boldsymbol{r}_{\boldsymbol{OBc_{semic}}}]\right) \tag{2.24}$$

4. Final inertia properties of Area 2 with respecto to $\sum_B$ consist of just

$$\overline{\overline{I}}^{B}_{Area2} = \overline{\overline{I}}^{B}_{trap} - \overline{\overline{I}}^{B}_{semic} \tag{2.25}$$

Rod inertia properties, with respect to its center, are readily known from Ginsberg (2008).

$$I_x^{c_{rod}} = I_z^{c_{rod}} = \frac{m_{LE}}{48}\left(3D^2_{LE} + 4b^2\right) \tag{2.26}$$

$$I_y^{c_{rod}} = \frac{m_{LE}}{8}D^2_{LE} \tag{2.27}$$

They are moved again by *Steiner's theorem*, equation A.31.

The total inertia tensor consists of the sum of previously computed inertia tensors with respect to $\sum_B$.

$$\overline{\overline{I}}_s^B = \overline{\overline{I}}_{Nut}^B + \overline{\overline{I}}_{Area1}^B + \overline{\overline{I}}_{Area2}^B + \overline{\overline{I}}_{LER}^B \tag{2.28}$$

For the proper definition of $\sum_P$, typical eigenvalue problem must be resolved so principal moments of inertia and their associated directions are known, (development available at Ginsberg (2008)).

$$\left| \overline{\overline{I}}_s^B - \overline{\overline{U}}\lambda \right| = 0 \tag{2.29}$$

being λ the eigenvalues of $\overline{\overline{I}}_s^B$. The 3 values of the eigenvalues founds are the principal moments of inertia ($I_{p_x}, I_{p_y}, I_{p_z}$), needed in equations (2.10)-(2.12), while the eigendirections will conform the principal axes of inertia frame $\sum_P$

Inertia properties of the seed are summarized in table 2.2. It is important to mention that inertia is non-dimensionalized as $\overline{I} = \frac{I}{\rho_s c^5}$. Inertia properties values are similar to the ones found by bibliographic research (Arranz et al., 2018b; Crimi, 1988; Ulrich et al., 2010; Lee, 2016).

$\overline{m}_s$	$\overline{I}_{p,x}$	$\overline{I}_{p,y}$	$\overline{I}_{pz}$	$\gamma\,[Deg]$	$\overline{x}_G^C$	$\overline{y}_G^C$
0.0615	0.0201	0.0017	0.0215	9.5797	-0.0186	0.1915

Table 2.2. Inertia properties of the seed model. $\overline{m_s}$ and $\overline{I}_p$ are the non-dimensional mass and principal moments of inertia, while γ corresponds to the angle that principals directions of inertia formed with respect to $\sum_C$, that is the deviation angle between $\sum_B$ and $\sum_P$.

2.2.3. Aerodynamic model

Aerodynamic forces and moments presented in motion equations must be obtained. Forces and moments are computed following a straightforward application of BET, similarly to Rao et al. (2014). By this theory, the blade is broken in individual and independent panels in which forces are computed by knowing the impinging velocity vector and therefore, the angle of attack. Then, total forces and moments are computed by summation of each contribution along the span. A pure application of this theory entails to neglect spanwise flow component, only considering horizontal and vertical wing velocity component at each blade or panel. Therefore, this is translated in spanwise forces neglected, which is a limitation of the theory. Actual winged-seeds will exhibit three-dimensional flow over the wing. Moreover, spanwise component is mainly linked to the Leading Edge Vortex (LEV) generated in actual samaras, which is presented by Lentink et al. (2009); Arranz et al. (2018a); Lee et al. (2014).

For the thesis particular case, computations are performed in $\sum_B$, and then they are translated forces to $\sum_L$ and moments to $\sum_P$, so they can be inserted in the previous equa-

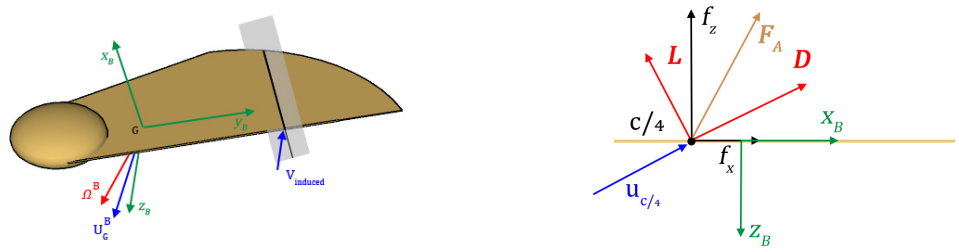

(a) (b)

Fig. 2.4. (a)Representation of seed's gravity centre velocity, angular velocity and the induced velocity impinging on a given blade element as a result of seed rotating. (b) displays a blade section with the consequent decomposition of aerodynamic forces in $\sum_B$

tions of motion (2.7)-(2.12). Wingspan was divided in N panels representing N number of blades. Aerodynamic forces and moments are computed in each blade independently and then integrated along the wingspan, as previously stated. This approach only resolves the force in the plane $x_B z_B$, neglecting force and velocity in spanwise direction y_B.

In order to compute the aerodynamic forces, the velocity at each panel must be known. However velocity changes along the chord in each span blade, so it was decided to compute a representative velocity for each panel at the quarter point of the chord in each panel. Therefore velocity:

$$\boldsymbol{u}_{c/4_i} = \boldsymbol{u}_{\mathrm{G}} + \boldsymbol{\Omega}^B \times \boldsymbol{r}_{G\,C/4_i} \tag{2.30}$$

where $\boldsymbol{r}_{G\,C/4_i}$ corresponds to the position vector that goes from seed's center of gravity to the quarter chord point of ith panel.

Neglecting spanwise component and simplifying notation, the velocity at the quarter chord point results in

$$\boldsymbol{u}_i = \boldsymbol{u}_{c/4_i} - (\boldsymbol{u}_{c/4_i} \cdot \boldsymbol{j}_B)\, \boldsymbol{j}_B \tag{2.31}$$

Previous equation (2.31) provides the velocity of the quarter chord velocity of each panel used for computations. Its module, which is essential for dynamic pressure of each blade, consist of $u^2(i) = u_i^2 + w_i^2$.

Lift and forces are computed by aerodynamic principles (Anderson Jr, 2010) .

$$\boldsymbol{L}(i) = \frac{1}{2}\rho_f u(i)^2 c(i) \Delta y\, C_L(\alpha(i)) \boldsymbol{t}_\perp \frac{u_i w_i}{||u_i w_i||} \tag{2.32}$$

$$\boldsymbol{D}(i) = \frac{1}{2}\rho_f u(i)^2 c(i) \Delta y\, C_D \boldsymbol{t}_\parallel \tag{2.33}$$

Lift and Drag are computed as the product of the dynamic pressure by the blade surface and the respective aerodynamic coefficients, taken from flat plate aerodynamics data from Dickinson and Gotz (1993) for $Re = 192$. Last terms are artificial vectorial terms in order to provide direction to lift and drag forces, where $\boldsymbol{t}_\perp$ is a unitary vector perpendicular to $\boldsymbol{u}_i$, direction in which lift acts. Moreover the fraction in (2.32) consist of a sign

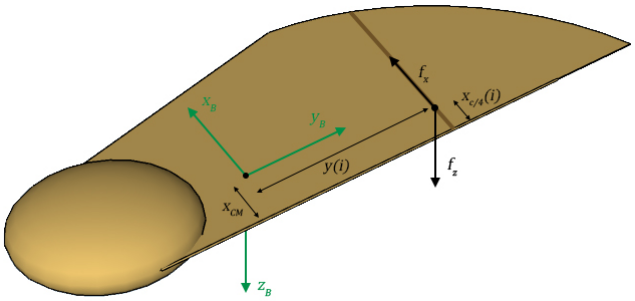

Fig. 2.5. Image of seed displaying forces and moment arm distances of aerodynamic moments for a given ith blade

function that switches the sense of the lift accordingly, depending on the sign of $u_i w_i$ .The other directional vector $\boldsymbol{t}_{\parallel}$ corresponds to the unitary vector parallel to velocity at quarter chord point, $\boldsymbol{u}_i$.

Lift and Drag forces are decomposed in each body coordinate.

$$f_x(i) = \boldsymbol{D}(i) \cdot \boldsymbol{i_B} + \boldsymbol{L}(i) \cdot \boldsymbol{i_B} \tag{2.34}$$

$$f_y(i) = 0 \tag{2.35}$$

$$f_z(i) = \boldsymbol{D}(i) \cdot \boldsymbol{k_B} + \boldsymbol{L}(i) \cdot \boldsymbol{k_B} \tag{2.36}$$

They are summed together to conform the total aerodynamic force.

$$\begin{bmatrix} F^B_{A_x} \\ F^B_{A_y} \\ F^B_{A_z} \end{bmatrix} = \begin{bmatrix} \sum_{i=1}^N f_x(i) \\ 0 \\ \sum_{i=1}^N f_z(i) \end{bmatrix} \tag{2.37}$$

Resultant aerodynamic force, expressed in $\sum_B$ and given by (2.37), are translated to $\sum_L$ frame so that they can be inserted into equations (2.7)-(2.9).

Moments are computed following a similar approach but in this case moment arm of previous forces for each blade is resolved.

$$\begin{bmatrix} T^B_x \\ T^B_y \\ T^B_z \end{bmatrix} = \begin{bmatrix} \sum_{i=1}^N f_z(i) y(i) \\ \sum_{i=1}^N f_z(i) \left(x_{\text{cm}} - \frac{c(i)}{4} \right) + \sum_{i=1}^N M_{c/4}(i) \\ -\sum_{i=1}^N f_x(i) y(i) \end{bmatrix} \tag{2.38}$$

where $(f_x, 0, f_z)$ correspond to force of each blade in $\sum_B$; y span distance from seed's center of gravity to ith blade; x_{cm} correspond to the distance from LE to seed center of gravity or center of mass; $M_{c/4}(i)$ conforms the quarter chord moment, constant for any angle of attack considering the quarter chord as the aerodynamic center, it was taken from Anderson Jr (2010) from a NACA 23012, in order to allow movement of center of pressure of samara which is essential for stability (in pitch) (Norberg, 1973). The quarter chord moment was computed as:

$$M_{c/4}(i) = \frac{1}{2} \rho_f u^2(i) c(i)^2 C_{m_{c/4}} \tag{2.39}$$

In the case of moments, moments given by (2.38) are again expressed in $\sum_B$. So they need to be changed to $\sum_p$ in order to be properly inserted in equations (2.10)-(2.12) .

In previous equations, fluid density has been considered constant, no compressibility effects are taken into account as the maximum velocity exhibited by the samara, at the wing tip, is well below the limit to consider variation, $M \sim 0.001$.

2.3. Numerical model

To solve the previous equations, a mathematical tool based in BET has been developed in Matlab. The numerical model is described in detail next, steps that the code follows is presented together with the different modules that can be distinguished.

First of all, as displayed in figure 2.6, Geometry is loaded. This module will provide all constant relative to samara geometry as well as physical constants present in the previous equation as: center of gravity, seed mass and total volume, inertia properties ...

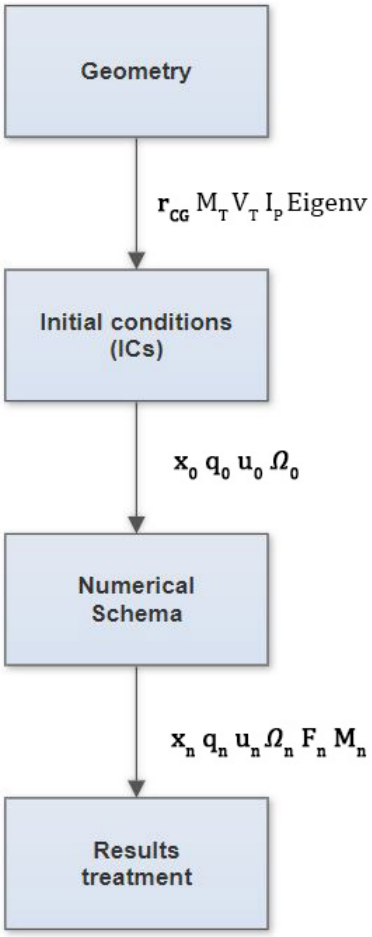

Fig. 2.6. Schematics representation of tool developed

Consequently, initial conditions (ICs) of motion are defined, which will be the starting point for the dynamical analysis. These conditions are defined so that initially $\sum_B$ and $\sum_L$ are parallel with their origins and axis y_B and y_L coincident. Furthermore, seed center of gravity starts at rest at the origin while an initial angular velocity Ω_0 in k_B is provided. This value of Ω_0 is well below the values found of Ω_{steady} in results section. This initial impulse is provided as a way of promoting samara entrance in autorotation.

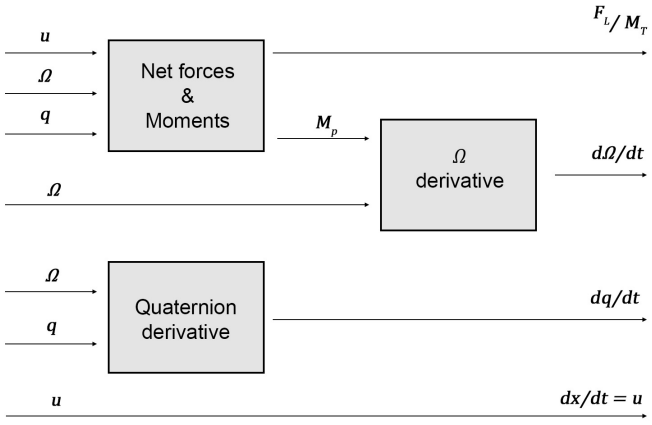

Fig. 2.7. Modular diagram of equations resolved by numerical method

In order for equations to be integrated (2.7)-(2.12) and (2.4)-(2.6), the 4th step Adams Basforth numerical method is implemented (LeVeque, 2007), explicit linear method. Although different schemas could have been implemented in each different equation of motion (while time progression is maintained across the different equations), it was decided to use the same Adams Basforth numerical method due to simplicity and lack of much computational advantage. The mumerical schema is depicted below for a generic variable U. Note that the method will required three initial steps to start the numerical schema, as presented in equation (2.40). Therefore, Euler method is applied to initiate the numerical schema.

$$U^{n+4} = U^{n+3} + \frac{\Delta t}{24}(-9f(U^n) + 37f(U^{n+1}) - 59f(U^{n+2}) + 55f(U^{n+3})) \tag{2.40}$$

2.4. Computational setup

This section is devoted to the set-up simulations. Parameters choice will be discussed and justified accordingly. Section 2.4.1 explains the time step selected for the simulations as well as numerical order of selected schema, while section 2.4.2 details a sensitivity analysis of the selection of the number of blades in which wing has been discretized.

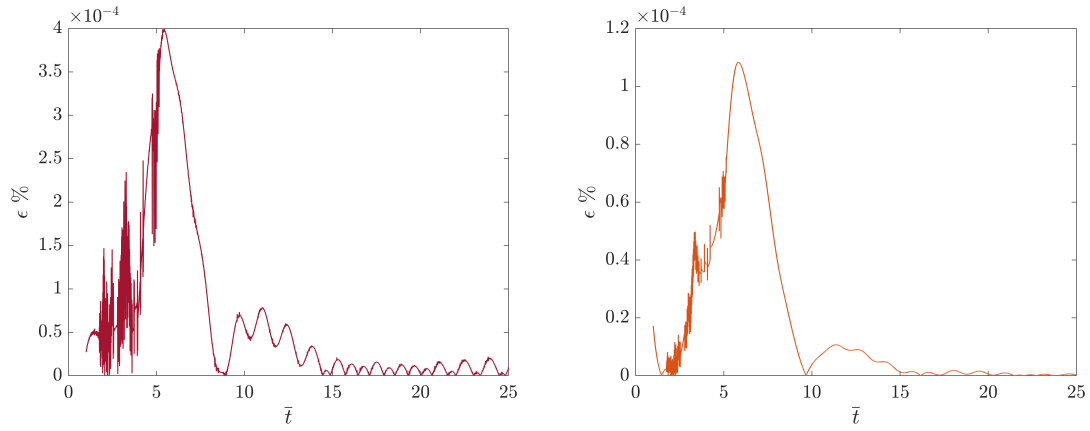

(a) (b)

Fig. 2.8. Errors percentage with respect to $\Delta t = 10^{-4}$. (a) Error for $\Delta t = 10^{-2}$ (b) Error for $\Delta t = 10^{-3}$

2.4.1. Timestep selection

Numerical schema developed for previous equations will depend on the timestep selection. Timestep will determine the accuracy of results as well as convergence if a not enough timestep is selected. Main interest will be to choose a timestep in which not enough accuracy is lost while not using an enormous timestep in order to save computational time. Therefore to properly address this decision, error for w_d will be calculated. As there is no analytical solution for the system, smaller timesteps with a higher one which will produce more accurate values. A reasonable interval will be $[10^{-1}, 10^{-4}]$. So $\Delta t = 10^{-4}$ was decided as the upper limit, so the results are compared with this upper bound. It is important to define the error as

$$\epsilon(\%) = \left| \frac{w_{d,i} - w_{d,10^{-4}}}{w_{d,10^{-4}}} \right| \cdot 100 \tag{2.41}$$

Error is computed with respect to results obtained using a higher time step value ($\Delta t = 10^{-4}$) due to the high numerical model complexity. Equations of motions (2.1)-(2.6) and (2.4) are coupled between them, then no analytical solution is available so error would be computed conventionally. This apparent limitation will be further discussed when order of accuracy is addressed.

From figure 2.8, it was found that for a value $\Delta t = 10^{-1}$, the numerical schema was not stable, so it was omitted. However, figure 2.8 displays errors associated with rest of timestep. First peaks appearing in figures correspond to errors associated to the unsteady behaviour leading to the stable autorotation. As it was expected errors for $\Delta t = 10^{-2}$ are higher that those for $\Delta t = 10^{-3}$. However peak errors are around 0.0004% and 0.0001% respectively, which are quite low. Comparing error values on steady state, errors are even lower. Therefore as error from $\Delta t = 10^{-2}$ can be considered quite small, this timestep is more than enough to use it in the numerical schema, as higher timestep does not provide

much numerical advantage but a considerable amount of computational time.

The numerical model developed in the current thesis is quite complex. It is composed of a considerable number of equation of motions coupled between them so no analytical solution is available. In order to solve approximately the system, the 4th step Adams Basforth numerical schema was used as stated in section 2.3.

This numerical schema must be validated accordingly. Main focus will be done on the order of accuracy. The order of accuracy quantifies the rate of convergence of a numerical approximation of a differential equation to the exact solution. Considering a general differential equation with u as the exact solution and u_{approx} as the approximation solution given by the numerical method, error will be defined as

$$E(\Delta t) = \left\| u - u_{approx} \right\| \leq C\Delta t^n \tag{2.42}$$

where the constant C will be independent of the selected timestep and usually depends on the solution u. So n corresponds to the order of accuracy of the numerical schema used to solve the differential equation. For further details about order of accuracy, reader is referred to LeVeque (2007).

One should validate the numerical schema developed in this project, order of accuracy of the results must concord with the one of a 4th step Adams Basforth numerical model. Due to the lack of an analytical solution, the error will be computed with respect to a higher time step, using equation (2.41). Taking steady average errors from the results obtained, an approximate order of accuracy of 1.16 is obtained, as displayed in the logarithmic plot, figure 2.9. Although the order of accuracy does not concord with the one corresponding with a 4th step Adams (4th order), the discrepancies are linked to non-linearities of the system resolved and the Euler steps applied to initiate the numerical schema.

2.4.2. Number of blades selection

Number of blades of the wing is a highly important parameter of the numerical model due to its influence in the final results. A higher number of blades will be translated to a higher accurate results. However, this priori advantage will come at the expense of more computational time again. The decision upon this parameter will be based on balance between accuracy and computational time. Therefore a sensitivity analysis is mandatory.

Figure 2.10 presents the variation of the results as the number of blades is changed. Subfigure 2.10a displays on the right axis the descent velocity while on the left, the seed's angular velocity. It can be observed that fewer blades will correspond to higher errors in the steady state, nevertheless, the error is not greater than 1.17%. Moreover, it is remarkable that neither descent velocity either angular velocity change from higher values of around 60 blades.

Subfigure 2.10b displays the influence of the number of blades on Tip speed ratio,

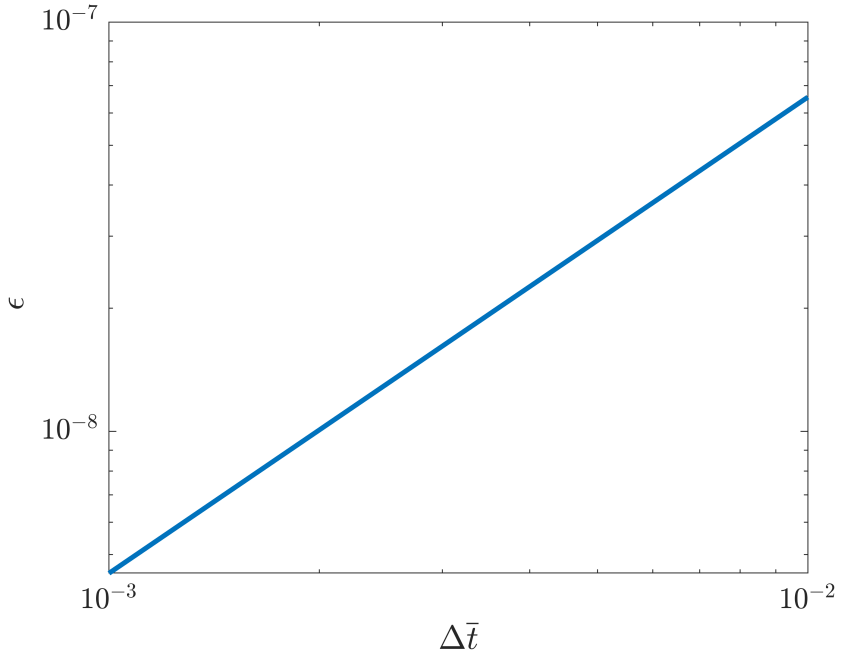

Fig. 2.9. Logarithmic representation of the error associated to timestep for the differential equations. The slope shows the order of the developed numerical method of the thesis

defined in equation (2.43). It is important to notice that tip speed ratio will follow the same tendency as before. Tip speed ratio is a compound variable composed by the ratio of the tip speed over the seed's descent velocity. Roughly this variable will determine how fast seed is actually spinning in comparison with seed's descent velocity. It was decided to include it in this sensitivity analysis as compound variables, by definition, will sum errors from their original variables. Therefore analysing error on tip speed ratio will yield a superior insight of the global error associated with the number of blades.

$$\lambda = \frac{r_t \Omega}{w_d} \tag{2.43}$$

where r_t is the absolute distance from the centre of gravity to the wing tip, w_d corresponds to descent velocity and Ω the rotational speed.

From previous subplot 2.10c, it can be inferred again that from a value of 60 blades errors tend to stabilize around 0.1%. So apparently there will no point on increasing this parameter further on as computational time will increase considerably. However it was decided to increase the number of blades up to 100, so tip effect is minimized (Seter and Rosen, 1992b) and therefore error will be reduced accordingly.

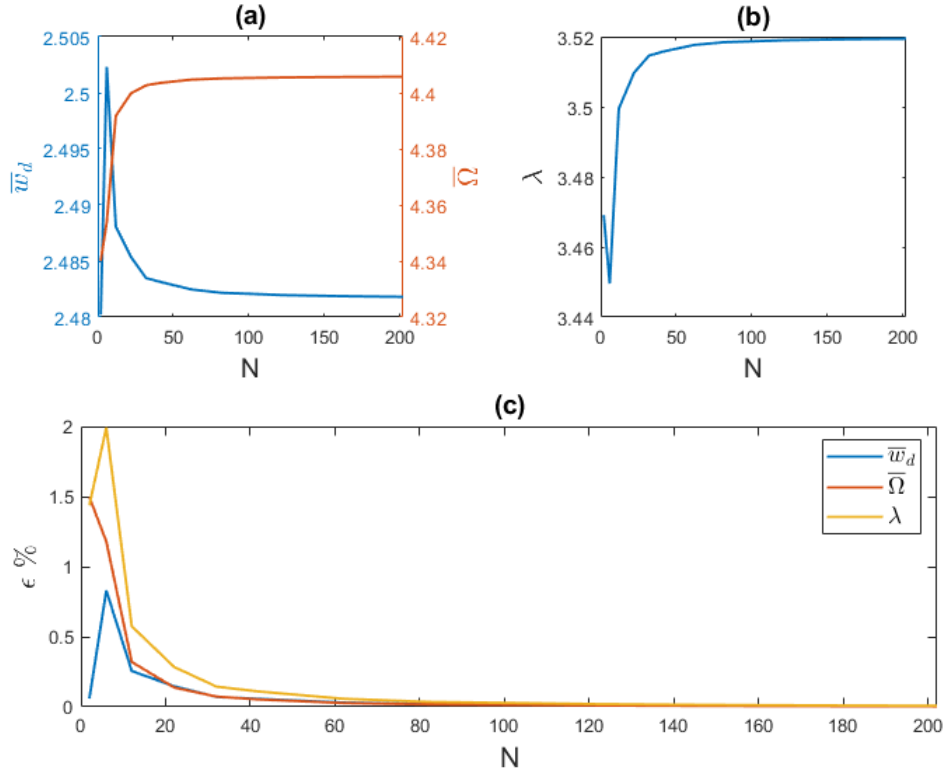

Fig. 2.10. Dependency of results on the number of blades N. (a) displays steady vertical descent velocity and angular velocity for different N while (b) shows the tips speed ratio as a function of N. (c) presents the error on the descent velocity, angular velocity, and tip speed ratio associated to N

3. RESULTS AND DISCUSSION

The problem under study is that of a samara with a fixed geometry of characteristic length, c and density, ρ_s immersed in a inviscid quiescent fluid of density, ρ_f and falling due to the action of gravity, $\boldsymbol{g}$.

Several simulations have been performed during this project in order to properly analyse inertia properties effect on the samara autorotation. During this chapter results and its discussion will be mainly presented.

Firstly, the non-dimensional problem is introduced in section 3.1 highlighting the important problem parameters. Secondly, section 3.2 treats preliminary simulations comparing them to the available bibliography. Lastly, in section 3.3, simulations regarding the analysis of inertia properties of the seed are discussed. Inertia properties are varied while maintaining constant the mass of the samara.

3.1. Non-dimensional problem and analysed parameters

Before any simulation is performed, the problem is non-dimensionalized. Any engineering problem has its associated magnitudes and their corresponding units. Nondimensionalization consists of partial or complete removal of the units by a suitable substitution of variables.

First, independent variables are selected. The geometry provides the characteristic length, c. The other physical variables of the problem are gravity, $\boldsymbol{g}$ and fluid density, ρ_f. Therefore, characteristic velocity can be defined as $v_c = \sqrt{gc}$, used in order to non-dimensionalized variables with time units. Therefore dependent variables result non-dimensionalized in: density ratio, $\varrho = \frac{\rho_s}{\rho_f}$; Inertia tensor, $\overline{I} = \frac{I}{\rho_s c^5}$; position, $\overline{\boldsymbol{x}}_G = \frac{\boldsymbol{x}_G}{c}$;time, $\overline{t} = \frac{t v_c}{c}$; velocity, $\overline{\boldsymbol{u}}_G = \frac{u_G}{v_c}$; forces, $\overline{\boldsymbol{F}} = \frac{F}{\rho_s v_c c^2}$ ...

Therefore, variables with units of time such as Ω can be non-dimensionalized with the characteristic velocity v_c as $\overline{\Omega} = \frac{\Omega c}{v_c}$. However, in order to be able to compare it with available bibliography, as in section 3.2, it will also be expressed in terms of the tip speed ratio, λ, defined in equation 2.43.

The attitude of the seed when it is autorotating might be investigated with the Euler Angles described in 2.1. However, this approach entails important drawback regarding the orientation of the principal axes of inertia since they are different. Comparison is not so intuitive and intermediate transformation steps will be required. One may think of quaternions. Yet, the same drawbacks as in Euler Angles approach will be faced. Therefore, the most intuitive approach to overcome this problem will be the definition of new angles between $\sum_B$, whose orientation is fixed, and $\sum_L$ that will describe perfectly

the seed attitude. These are the flight angles, as explained below in section 3.1.1

3.1.1. Flight angles

Three flight angles are defined to completely determine the attitude of the seed, similarly to the Euler Angles. These angles are construed between the $\sum_B$ and $\sum_L$, commonly to every seed simulated.

The angles are:

- precession angle, ψ, measuring the angle of rotation of seed with respect to to z_L;
- coning angle, β, which indicates the inclination of the wing seed with respect to the horizontal plane;
- pitch angle, θ, similar to a geometric angle of attack

For clarification, assume that the wing seed lies on the horizontal plane $x_L y_L$. This configuration will lead to flight angles of $\beta = \theta = 0$ while ψ might have any value. if a rotation around x_B is applied, wing seed will no longer remain in the horizontal plane. The angle that will be formed between this horizontal plane and y_b will be the coning angle, β. On the contrary, if rotated around y_b, the rotated angle will constitute the pitch angle, θ.

Although the same nomenclature as Euler angles has been used, a prime symbol has been omitted so there is no confusion. Mathematically, flight angles were computed as next with the aid of quaternions. Precession angle is computed from the projection of $\boldsymbol{j}_b$ onto the horizontal plane $Ox_L y_L$

$$\psi = \tan^{-1}\left(\frac{\mathbf{j}_b \cdot \mathbf{j}_L}{\mathbf{i}_b \cdot \mathbf{i}_L}\right) \tag{3.1}$$

Coning angle is computed with the projection of $\boldsymbol{j}_B$ onto the vertical axis z_L.

$$\beta = \sin^{-1}\left(\mathbf{j}_b \cdot \mathbf{k}_L\right) \tag{3.2}$$

The computation of pitch angle requires to define a new intermediate vector, $\boldsymbol{e}_\perp$, which is perpendicular to $\boldsymbol{j}_B$ and is contained in the horizontal plane; then, $\boldsymbol{e}_\perp = \boldsymbol{k}_L \times \boldsymbol{j}_B$

$$\theta = \cos^{-1}\left(\mathbf{i}_b \cdot \mathbf{e}_\perp\right) \tag{3.3}$$

Convention of sign for θ, according to the previous definition, is that θ will have positive when the wing has a positive angle of attack. This is translated when the seed is rotating with $\boldsymbol{\Omega} = \Omega\, \boldsymbol{k}_L$, θ sign will be determined from the dot product $e_\perp \cdot \boldsymbol{k}_B$. So that when scalar product >0, the pitch will be negative, $\theta < 0$, and vice-versa. Therefore, according to this convention, stable simulations results in negative pitch angles. Nevertheless, pitch angle are presented positively in next sections only for representative purposes.

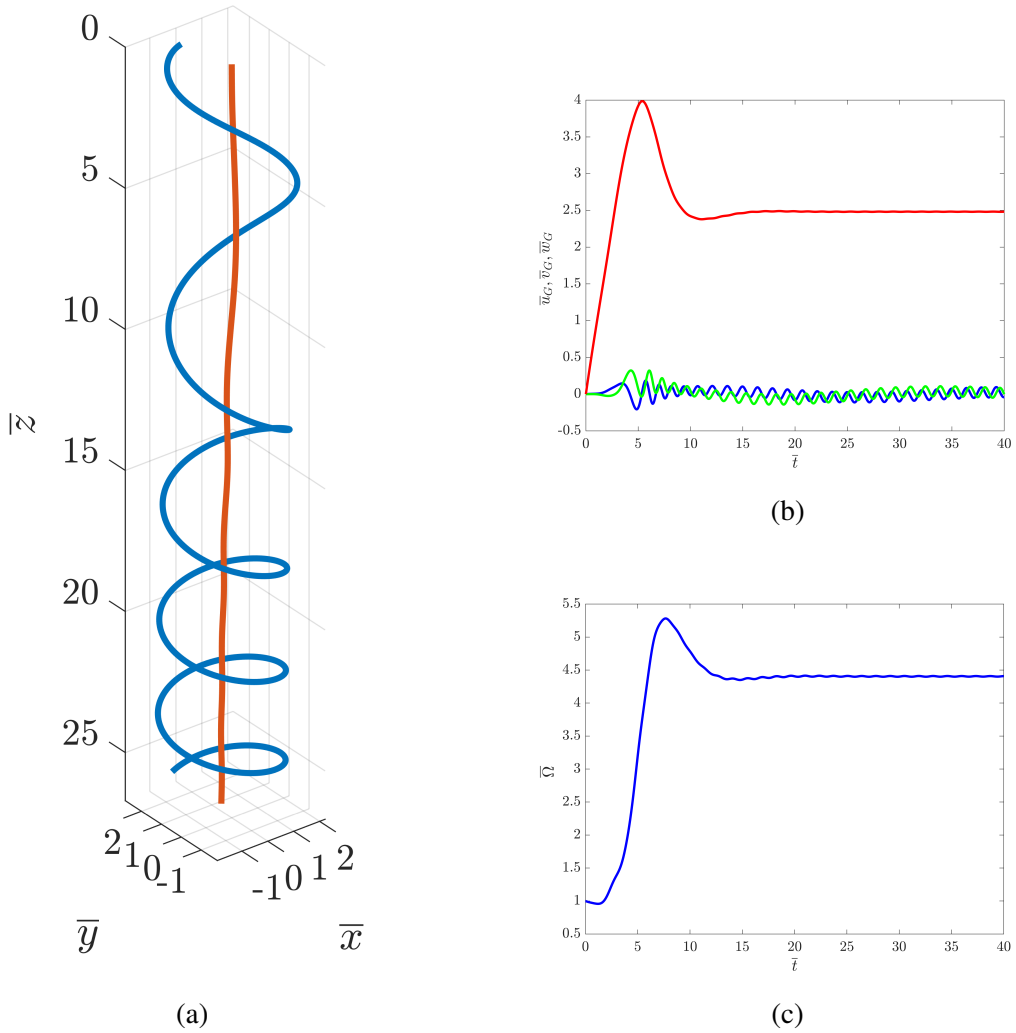

(a) (b) (c)

Fig. 3.1. Representation of baseline simulation, defined geometry with LER. a) (—) trajectory of seed's center of gravity, (—) tip trajectory. (b) Seed's velocity: (—) $\overline{u}_G$; (—) $\overline{v}_G$; (—) $\overline{w}_G$. (c) Angular velocity, $\overline{\Omega}$

3.2. Preliminary simulations

In this section, different simulations are presented and compared with the bibliography available. Firstly, the original seed model with and without LER are introduced. Moreover, general values of seed autorotation are contrasted with available literature data so numerical results can be validated.

Figures 3.1 and 3.2 display the temporal evolution of the main variables of motion for the baseline simulation. Transient is very well distinguished in every figure by the associated peaks in the different variables of motion until stable steady autorotation is achieved. Steady average values are lower than the unsteady values and are independent of the initial rotational impulse given to the samara.

The trajectory is represented in 3.1a for the interval of time $\bar{t} \in [0,10]$, exhibiting the

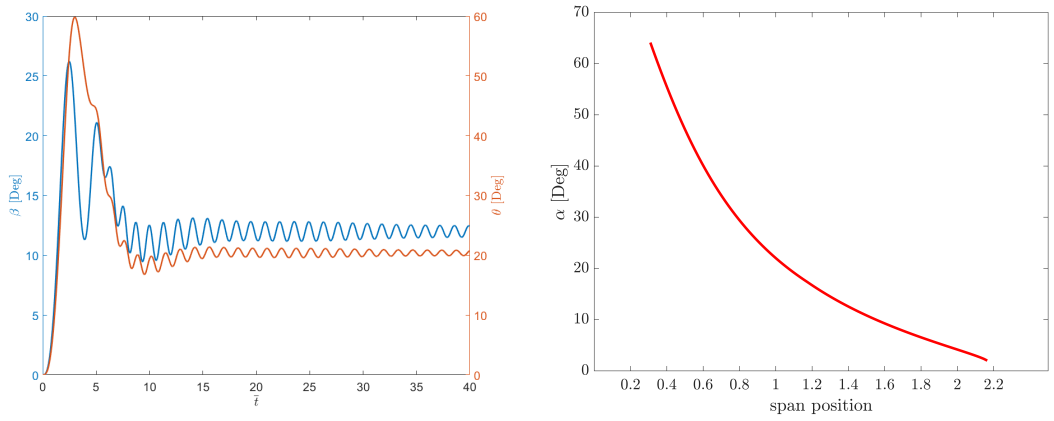

(a) (b)

Fig. 3.2. Flight angles of baseline simulation. (a) flight angles: (—) coning angle, β; (—) pitch angle, θ. (b) Effective angle of attack along span

characteristic helicoidal motion described by the wing tip. Furthermore, it is observable, even in such reduced time domain, the slight relative displacement and rotation of the seed's gravity center. In the absence of any perturbation, seed's center of gravity rotation in horizontal plane is attributed to the different position of the center of gravity and center of rotation, which are close one to another but do not coincide (Azuma and Yasuda, 1989; Norberg, 1973). Moreover, this behaviour can be noticed in figure 3.1b. $\boldsymbol{u}_G$ and $\boldsymbol{v}_G$ slightly oscillate as a consequence of the induced velocity experienced by the seed's center of gravity when rotation axis is displaced away of gravity center, $\Delta u_G = \Omega\, r_{CG}$, where r_{CG} consists of the distance from the axis of rotation to the center of gravity. Regarding vertical velocity, w_G exhibits a large peak transient until steady is achieved leading to seed to fall at a constant speed, w_d

The seed will tend to rotate with respect to a vertical axis of rotation, seed rotating approximately in a horizontal plane. As a consequence, angular velocity modulus, represented in figure 3.1c, could have been approximated as $\boldsymbol{\Omega} = \Omega \boldsymbol{k}_L$, as vertical component will be its main contribution, neglecting the other components. Angular velocity departs from the initial value, given as the initial impulse. Then, it will increase exhibiting the peak associated with transient until stabilizing once stable autorotation is reached. Oscillations in steady are linked to the motion of the center of rotation that will oscillate periodically (Arranz et al., 2018b).

Regarding the flight angles, figure 3.2a, similar peaks of unsteady transition are found. However, flight angles exhibit an oscillation in the steady with the same period as the seed angular velocity, $T = \frac{2\pi}{\Omega}$. Therefore, nominal flight angles are obtained from averaging over the last period. Moreover, changes in nominal values over time is the result of the center of rotation motion (Arranz et al., 2018b).

Figure 3.2b presents the effective angle of attack of flow impinging on the wing along the span. This values will oscillate modestly as flight angles do but distribution will be

preserved as seed rotates.

Steady averaged values obtained for the model developed in the present thesis are summarized in table 3.1, together with available literature empirical data of different species. Data from bibliography has been presented non-dimensionalized in order to ease the comparison. Although Reynolds number of performed simulations cannot be computed due to inviscid flow nature, an estimation might be assumed considering viscosity of air with the simulation data obtained, yielding values of Reynolds around 1500. It is remarkable how both simulated seeds would fall in the Reynolds number of the empirical data. With respect to the variables of motion, empirical data spread in a wide interval that englobes the simulations performed. The large spreading of sample is mainly based on the different species, each one with different geometrical properties. Moreover, inside a species, differences in geometry are also found, seeds differing somehow in size, platform or any other aspect. So autorotational winged seeds entail a big group, with a considerable range of geometrical properties, which are translated also in a wide interval of motion data. On the other hand, the designed model has its limitations, as it will be discussed further on, mainly due to the aerodynamic module with a considerable amount of assumptions and simplifications. These limitations range from assumptions of no spanwise flow to a minor planar assumption, for example, the effect of wing ribs which is not taken into account. Yasuda and Azuma (1997) compared the motion of a real samara with artificial ones, one with ribs and another one without. They discovered that that seeds without ribs roughness had greater descent velocity and lower spinning rate.

On the other hand, the difference between the performance of seed with and without Leading Edge was firstly treated by Varshney et al. (2011). Seeds whose LE was removed have a higher falling rate and higher descent velocities (Varshney et al., 2011). Present simulations confirmed that trend. Regarding geometrical properties of the model, Inertia of seed without LER had lower inertia while the center of mass is displaced rearwards, placed below y_n axis.

Source	Species	Re	$\overline{w}_d$	$\overline{\Omega}$	λ	β	θ	$\overline{R}_{gyration}$
Present simulation (with LER)	-	-	2.48	4.41	3.52	12.01	20.40	0.016
Present simulation (without LER)	-	-	2.51	4.53	3.71	39.79	40.68	0.042
Arranz et al. (2018b)	-	240	3.01	4.76	2.96	10.06	13.06	0.008
	-	160	3.24	4.37	2.52	11.49	15.82	0.012
	-	80	3.89	3.54	1.66	15.72	24.77	0.027
Green (1980)	*Acer saccharum (Sugar Maple)*	1673	2.30	6.73	3.31	9	5.8	-
	Acer negundo (Boxelder)	1833	2.08	6.14	3.17	12	12.6	-
	Acer rubrum (Red Maple)	723	1.49	5.96	2.89	36.3	12.5	-
	Acer saccharinum (Silver Maple)	1880	1.96	4.47	4.29	27.3	10.6	-
Azuma and Yasuda (1989)	*Acer palmatum Thunb. Var*	1405	2.35	5.21	2.27	27.6	1.39	-
	Acer palmatum Thunb	1473	2.46	8.54	2.04	15	0.90	-
Salcedo and Vargas (2013)	*Swietenia macrophylla (Mahogany)*	2302	3.27	2.38	1.55	20	-	-
Yasuda and Azuma (1997)	*Acer diabolicum Blume*	-	2.03	4.73	-	10	0	-
	Artificial	-	2.80	3.22	-	12	2	-

Table 3.1. Average values of the kinematics (Re, $\overline{w}_d$, $\overline{\Omega}$, λ, β, θ, $\overline{R}_{gyration}$). For comparison, the table gathers experimental values from the existing literature for different species.

Previously it is said that the center of rotation is close to seed's center of gravity but they do not coincide. Hence it seems reasonable to compute the axis of rotation which is defined as the line parallel to $\mathbf{\Omega}$, about which all points of the seed are in pure rotation. From Ginsberg (2008)

$$\mathbf{x}_{ICR} = \frac{\mathbf{\Omega} \times \mathbf{u}_G}{\Omega^2}, \tag{3.4}$$

where $\boldsymbol{x}_{ICR}$ is a vector perpendicular to $\mathbf{\Omega}$ which goes from $\boldsymbol{x}_G$ to the closest point of the axis of rotation. Therefore radius of gyration is defined as this distance which mathematically is translated into the vector module of $\boldsymbol{x}_{ICR}$ simply as

$$\overline{R}_{gyration} = \sqrt{\overline{x}_{ICR}^2 + \overline{y}_{ICR}^2 + \overline{z}_{ICR}^2} \tag{3.5}$$

3.3. Inertia parametric study

In this last section, the effects of inertia on the autorotation of the samara model are treated in detail. However, due to the nature of the problem which consists of a couple between seed's inertia and aerodynamic forces (Varshney et al., 2011), it is difficult to isolate the contribution of inertia to the autorotation motion, as both feed and are consequence of the motion. In addition to the previous items, the position of seed's gravity center must be included in the problem analysis due to the huge contribution in moment equations (2.10)-(2.12) and consequently on the motion (Norberg, 1973).

As a consequence of the difficulties, addressing inertia properties seems complex. First, it was thought to impose different inertia tensors and try to obtain the corresponding geometry by inversion. However, inverting process is not so straight and might lead to unrealistic cases, impossible geometries or even multiple geometries. So it was decided to

perform a parametric study by which inertia properties are changed maintaining as much of possible of the geometry of the baseline seed, isolating inertia effect on autorotation. In order to do so: total seed's mass and seed platform are maintained constant so that both gravity force and aerodynamic module are preserved in the study.

Once constraints are defined, the first case analysed corresponds to the displacement of the Eeading Edge Rod. While the second case, the Leading Edge Rod mass contribution is varied while changing nut mass in the same quantity, preserving total mass. In both cases, only seed's inertia properties and center of gravity are altered as a consequence of the parametric study.

3.3.1. Displacing Leading Edge Rod

In this first analysis, Leading Edge Rod is displaced in a wide domain with respect to $\sum_C$, translating it both in $\boldsymbol{i}_B$ and $\boldsymbol{j}_B$ directions, chordal and spanwise directions. Position of LER will be expressed in terms of the position of this rod center of mass. Furthermore, displacing the LER entails not only the variation of the inertia tensor but the displacement of the seed's center of gravity, taken into account in the analysis.

Therefore, the parametric study is performed in a rectangular domain of $0.3x0.5c$ with a size grid of $\Delta\bar{x}_{LER} = 0.015c$, $\Delta\bar{y}_{LER} = 0.025c$, yielding the following results.

On one side, the relevant variables of motion of the samara are represented in figure 3.3. Different values of each variable are represented with a contour level. Moreover, a red line is represented corresponding to the most rearward position of LER so that seed's center of gravity lies on the interval of stable autorotation according to Norberg (1973). It is highlighted that the chordal direction corresponds to the most sensitive directions to LE displacements.. However it is remarkable that displacing LER in the spanwise direction will have its contribution, levels have a modest slope and possibly due to coupling.

In addition, unstable frontier was found around a rearward displacement of $0.22c$ with a jagged profile, as a consequence of the mesh selected ($\Delta\bar{x}_{LER} = 0.015c$, $\Delta\bar{y}_{LER} = 0.025c$). When approaching this frontier the variables of motion exhibited large variations characteristically of unstable regimes.

From a general point of view, it can be inferred general trends of the motion variables. Figure 3.3a shows a parabolic behavior of the descent velocity, a minimum was found at a rearward displacement of 0.2c, while it will increase until unstable frontier is reached. However, angular velocity displayed in figure 3.3b, shows a continuous reduction in spinning rate as LER is translated backward falling catastrophically, not able to sustain autorotation. Consequently, tip speed ratio, as displayed in figure 3.3c has a composed behavior of the previous variables. Tip speed ratio followed a parabolic trend with an optimal around $\Delta\bar{x}_{LE} = 0.2$. On the other side, radius of gyration will exhibit a different trend, contour 3.3d showed concentric levels with a similar contribution to the displacement of LER in both directions. This will also be seen at figures 3.7 , when

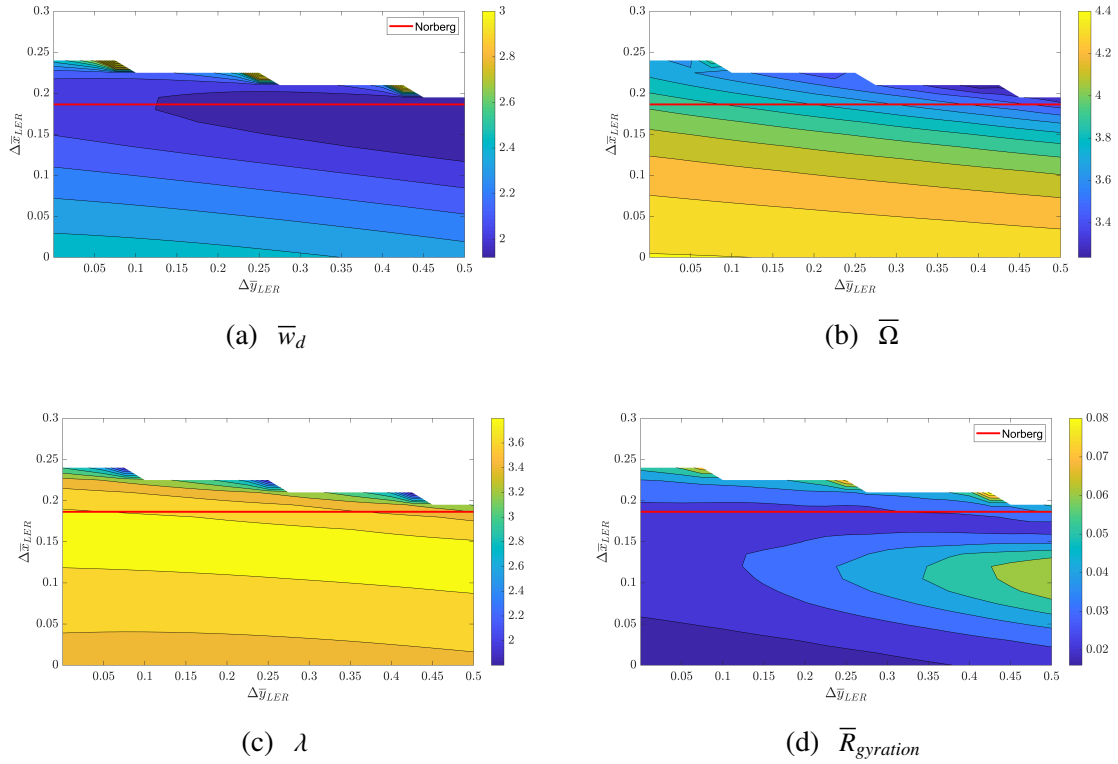

(a) $\overline{w}_d$ (b) $\overline{\Omega}$

(c) λ (d) $\overline{R}_{gyration}$

Fig. 3.3. Changes on steady average values of variables of motion as LER is displaced. (a) vertical descent velocity, $\overline{w}_d$. Subfigure (b) Angular velocity contour, $\overline{\Omega}$. (c) tip speed ratio, λ. (d) Radius of gyration, $\overline{R}_{gyration}$

analysing seed's trajectories.

With respect to the flight angles, they follow similar tendency displaying higher sensitivity as LE rod is displaced in the chordal direction, as it can be seen in figure 3.4. These angles tend to grow similarly suggesting a possible coupling between them. Moreover, this coupling trend it is highlighted as both flight angles tends to reach similar values when approaching the unstable frontier.

Before immersing the reader into the inertia variation study, variations of the seed's center of gravity must be addressed, as displacement of the center of gravity is expected to account partially for the variation of the seed's autorotation. While LER is displaced in a rectangular domain of $0.3x0.5c$, Seed's c.g displacement will result in $0.03x0.05c$. However these apparent small displacements of the seed's center of gravity affect considerably the autorotation motion. In order to check that affirmation, simulations outside of the stable envelope were carried out imposing the seed's gravity center of the baseline case, initial position of center of gravity. Simulations showed that stable autorotations were achieved for previous values of inertia for which autorotation was not reached, confirming that seed's gravity center is coupled in the problem as well.

Moreover, other simulations were performed trying to quantify the contribution of the seed's center of gravity displacement to the total motion variation. Therefore, rough numerical computations were performed to compute the percentage of change of variable

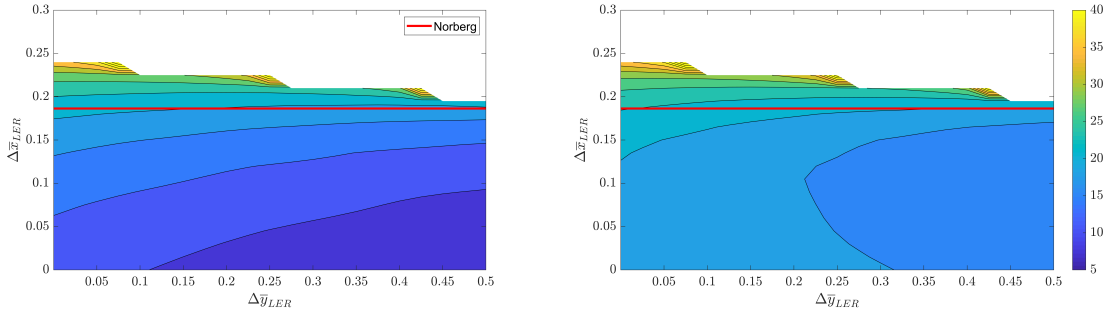

(a) β (b) θ

Fig. 3.4. Steady average flight angles contours displacing the LER. (a) coning angle contour, β. (b) pitch angle, θ

of motion due to seed's center of gravity displace cement and inertia changes. In order to do so, simulations were performed with seed's center of gravity fixed (with its original value), while inertia properties have values corresponding to the simulation performed, inertia properties of the point of domain. In that way, the only thing that varies is the inertia properties of the seed. Computations were performed by computing the percentage of variation between the cases with seed's center of gravity fixed and the nominal one. These computations suggested a contribution of 30 % of the total change on motion variables due to center of gravity translation. Nevertheless, these results have no validity and they only intend to provide some understanding on the level of contribution of both inertia and seed's center of gravity to autorotation.

Inertia properties must be displayed to understand its contribution. Therefore they were presented with respect to $\sum_C$, in percentage of variation with respect to the baseline properties. Therefore, they are plotted in figures 3.5. They exhibited the expected behavior. Inertia in axis x will be affected only by displacing LER in y direction while I_y similarly in x. In spite of the consequences of their similar definition, I_x is more altered as seed's inertia in y consist of a lower value and therefore being more susceptible in percentage to change over its baseline value. Moreover, this is remarkable when analyzing inertia in z axis. I_z is changed in both directions as, by definition, it is the sum of the square of the modulus vector position of mass and as LE is displaced in both directions, the contour will result in a parabolic shape. The last inertia tensor component left to be treated is the cross-product of inertia. I_{xy} is varied in both directions ranging from a 40% increase to an almost null value in the non-stable zone. Cross product contour suggests a possible relation with samara autorotation stability, better observed when looking at the convergence of the flight angles and the angle of the principal directions of inertia.

The most remarkable finding is the one displayed in figure 3.6 showing the behavior of the angle between principals of inertia and body reference frames. Unstable frontier fell following a level of 5^o implying a huge contribution of the angle of the principal directions of inertia. The discovery would suggest that the angles of the principal direction will be one of the main contributions of the coupling phenomena together with the seed's center

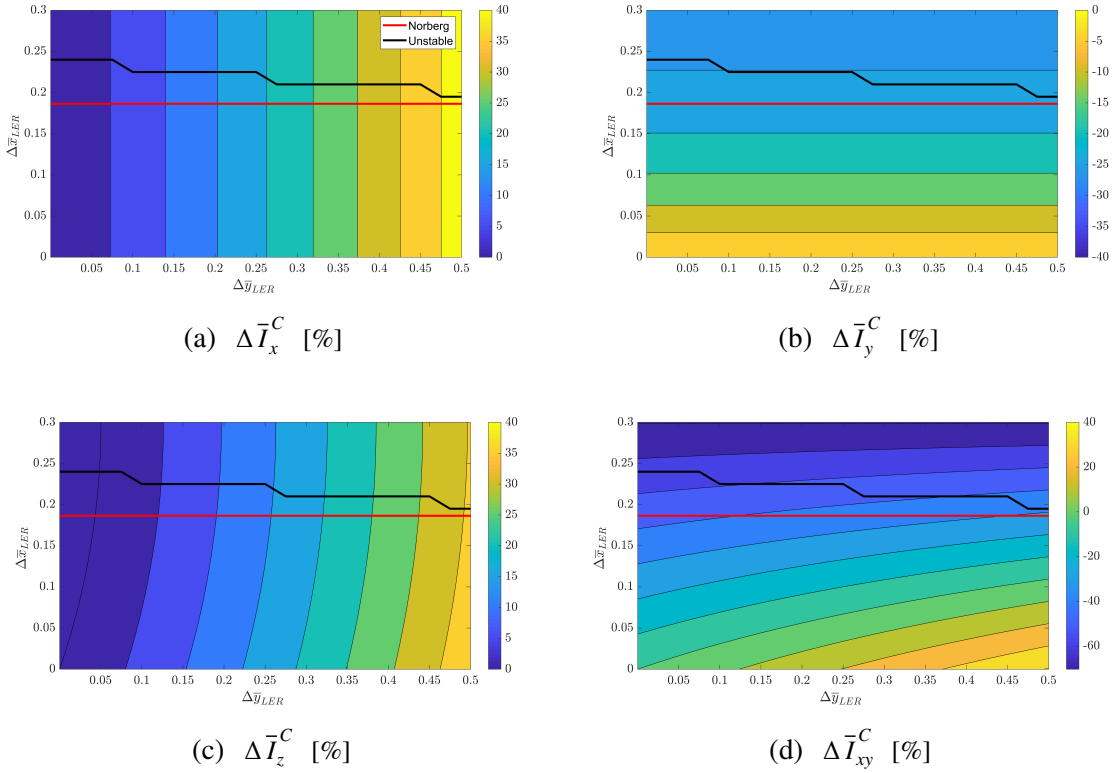

(a) $\Delta \bar{I}_x^C$ [%] (b) $\Delta \bar{I}_y^C$ [%]

(c) $\Delta \bar{I}_z^C$ [%] (d) $\Delta \bar{I}_{xy}^C$ [%]

Fig. 3.5. Contours displaying changes in percentage of the tensor of inertia with respect to its original position as LER is displaced. Inertia is computed with respect to nut center $\sum_C$. (a) Inertia in axis x_C. (b) Inertia in axis y_C. (c) Inertia in axis z_C. (d) cross product of inertia xy_C

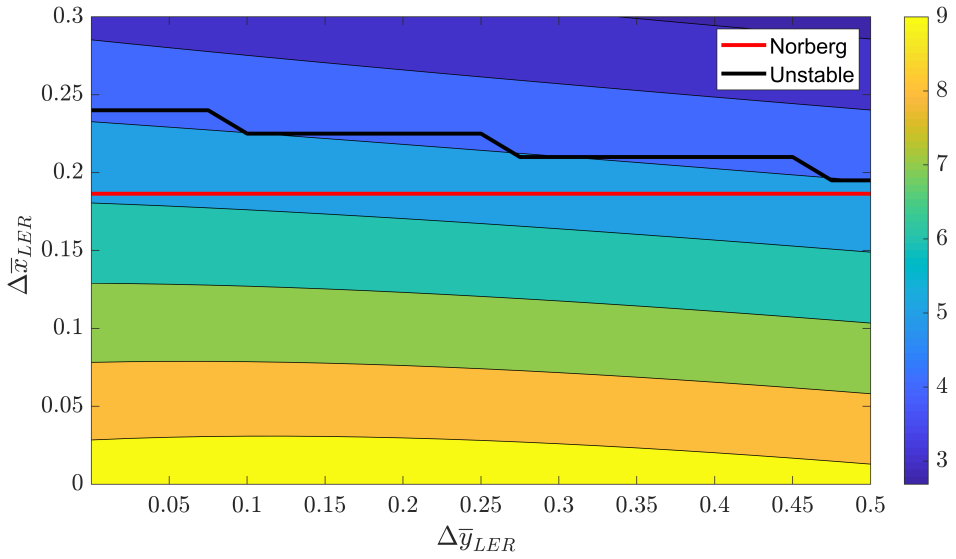

Fig. 3.6. Contours of angle that forms the principals direction of inertia with respect to $\sum_B$ as LER is translated

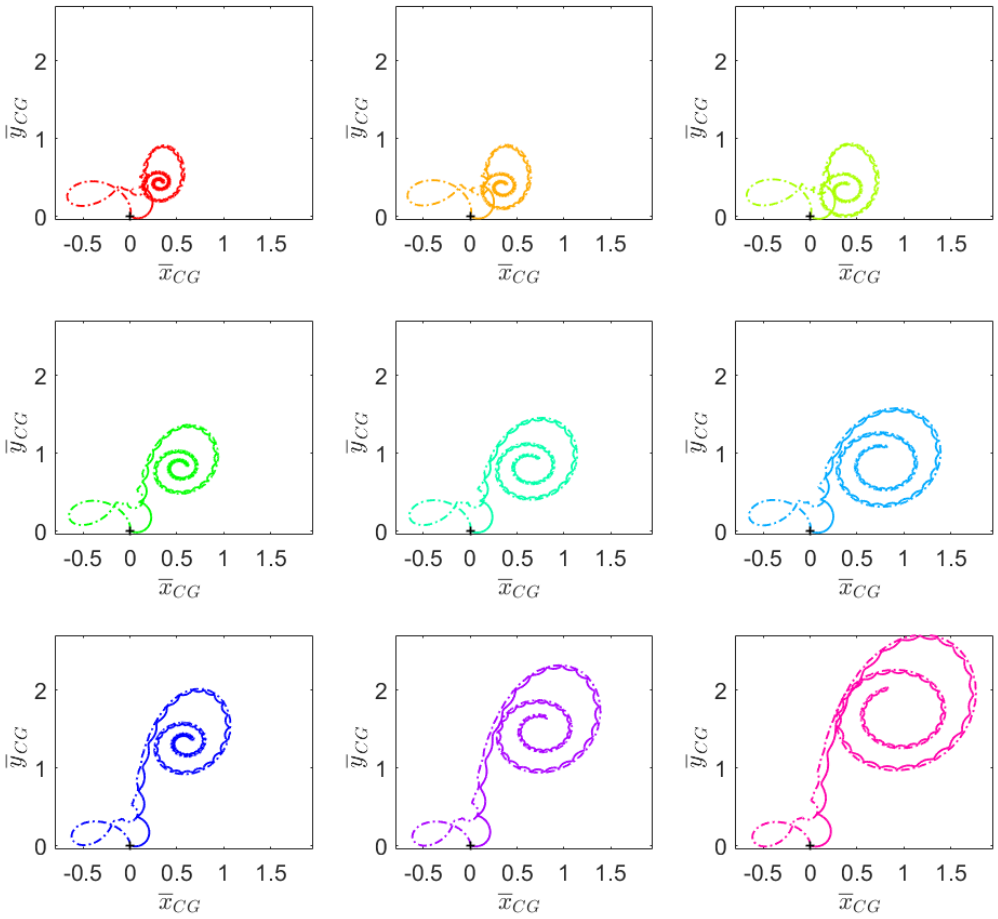

Fig. 3.7. Different trajectories together with their ICR as LE is displaced. (—) seed's gravity center baseline trajectory; (– · –) ICR evolution. Trajectories are distributed such as when moving in the vertical direction, LE is displaced $\Delta x_{LE} = 0.045c$ each figure, while moving to the right will be translated in a LE displacement of $\Delta y_{LE} = 0.075c$ similarly

of gravity.

Trajectories of seed's center of gravity are presented by projections onto the horizontal plane, together with their ICR positions. They are displayed following a pattern in figure 3.7. It is remarkable the unsteady process in which ICR separates from the seed's c.g. From trajectories, it can be inferred that displacing LER in the spanwise direction will result globally in a higher covered area until autorotation. In case of moving LER in the chordal direction, transient leading to stable autorotation will require high horizontal displacement before reaching stable autorotation with respect to a point.

Forces and moments must be analysed. Therefore, it is important to define the aerodynamic coefficients. These coefficients will consist of the non-dimensionalization of aerodynamic forces expressed in $\sum_B$ with a reference dynamic pressure and the wing surface of the seed.

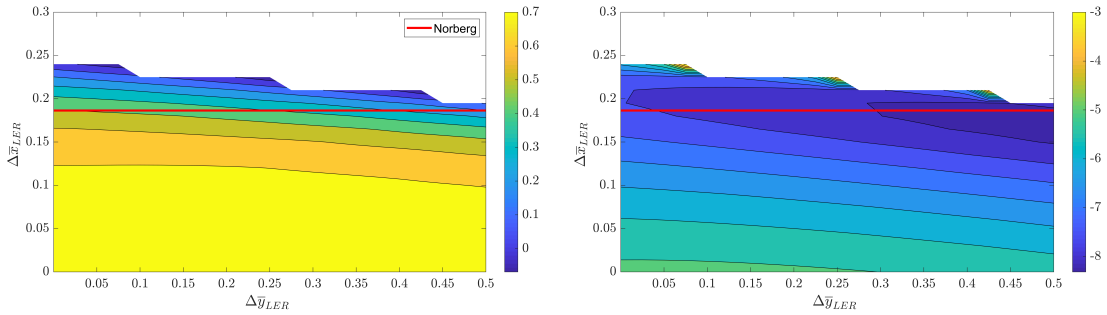

(a) CF_x^B (b) CF_z^B

Fig. 3.8. Contours of forces in $\sum_B$ as LER is displaced. (a) Force in x_B. (b) Force in z_B

$$CF_x^B = \frac{\boldsymbol{F}_A \cdot \boldsymbol{i}_B}{\frac{1}{2}\rho_f w_d^2 S} \qquad CF_z^B = \frac{\boldsymbol{F}_A \cdot \boldsymbol{k}_B}{\frac{1}{2}\rho_f w_d^2 S} \tag{3.6}$$

Forces as plotted in figures 3.8, presented similar trends as variables of motion. Both coefficients will display higher sensitivity of LE displacing in x direction, while varying modestly in the other direction. Nevertheless, while CF_x^B tends to be reduced as unstable frontier becoming null at it, CF_z^B will have different behaviour. Vertical seed force will increase reaching a maximum, that will explain the reduction in the descent speed, then will fall catastrophically until frontier is reached. From this analysis, it can be inferred that no autorotation will be possible when no force in the wing plane is generated. Consequently, as the pitch angle is small, it may be assumed that force in the horizontal component is required for autorotation. From physical sense, this hypothesis seems feasible as the seed will require horizontal component force to sustain forward motion and rotate. However, this will be needed to be proven accordingly.

Regarding seed's moments, similar approach was executed. Aerodynamic moment coefficients were defined as:

$$CM_x^B = \frac{\boldsymbol{M}_A \cdot \boldsymbol{i}_B}{\frac{1}{2}\rho_f w_d^2 S\, c} \qquad CM_y^B = \frac{\boldsymbol{M}_A \cdot \boldsymbol{j}_B}{\frac{1}{2}\rho_f w_d^2 S\, c} \qquad CM_z^B = \frac{\boldsymbol{M}_A \cdot \boldsymbol{k}_B}{\frac{1}{2}\rho_f w_d^2 S\, c} \tag{3.7}$$

The moments behaviour will tend to be again similar as before. While CM_x^B and CM_y^B will grow until a maximum is reached and then decrease until frontier, CM_x^B will reduce until zero at the unstable border, suggesting what is logical: the moment component in z as a requirement for autorotation as the seeds rotate almost horizontally and which axis of rotation can be approximated as vertical axis, in z_l.

3.3.2. Modifying Leading Edge Rod mass

The last analysis of inertia will consist of a different approach. This time the rod is fixed at its original position at the leading edge (see section 2.2.1). Mass of rod will be varied

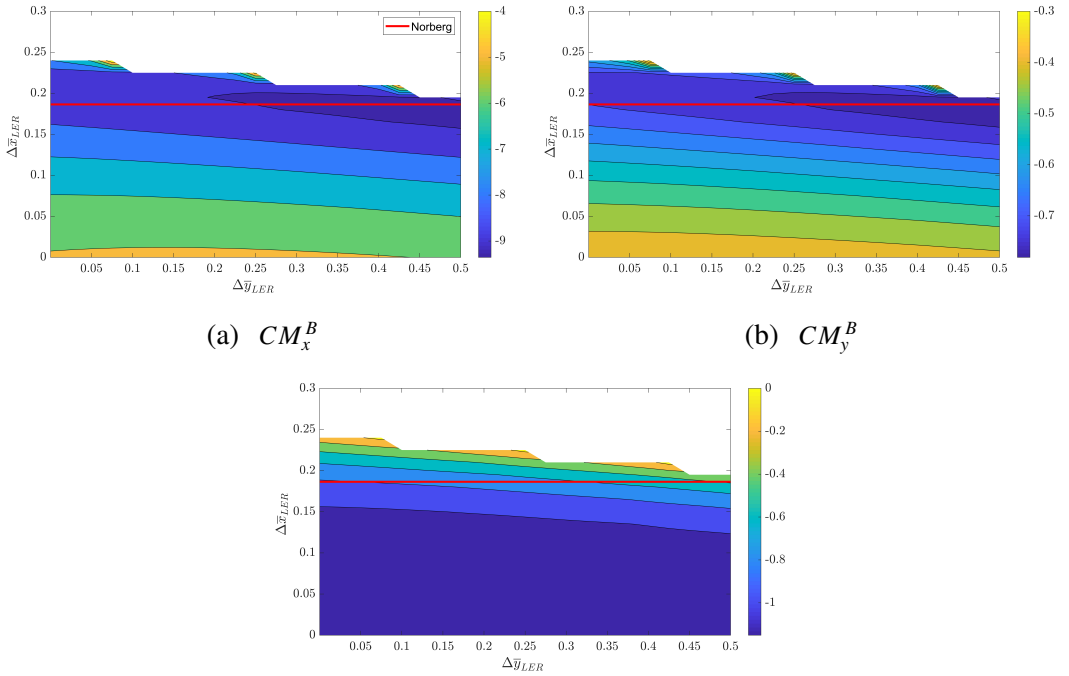

(a) CM_x^B (b) CM_y^B

(c) CM_z^B

Fig. 3.9. Contours of moments in $\sum_B$ as LER is displaced. (a) Moment in x_B. (b) Moment in z_B

from its original value by varying the nut one in the same amount so total mass seed m_s is conserved. In order to accomplish it, densities of rod and nut are tuned accordingly.

Characteristic variables of motion are plotted in figures 3.10. It is important to point that a black circle is presented in plots highlighting the baseline geometry. Descent velocity at figure 3.10a displayed a maximum when no rod is present in the model, decreasing until a minimum point at $\overline{m}_{rod} = 2.5\,\%\overline{m}_s$, from this point on, speed will increase again tending to stabilize around a constant value. Angular velocity behaviour, visible at figure 3.10b, exhibits a parabolic behaviour, reaching a minimum around $5\%\,\overline{m}_s$ and continuing to increase almost *linearly* as rod mass raises. The composed variable of previous tip speed ratio in figure 3.10c shows similar but reversed behaviour compared to descent velocity. It reaches a maximum at $2.5\%\,\overline{m}_s$ decreasing and stabilizing around values of 3.46. Although from the behaviour of the descent speed and angular velocity, tip speed ratio is expected to increase instead of stabilizing. The stabilization is the consequence of center of gravity displacing in the span direction, reducing the distance from the center of gravity to tip. On the other hand, sharp peaks are due to large variations of motion variables in that interval, higher refinement should have been used. Radius of gyration displays a hyperbolic shape. The radius is maximum as no rod is present in the geometrical model but decrease drastically and stabilizing as rod contribution raises.

Flight angles, displayed in figure 3.11, describes a similar trend as the radius of gyration. Both coning and pitch angles depart from their maximum values when no rod is present and tend to reduce similarly until the stabilization trend is exhibited for high contribution mass values of the rod.

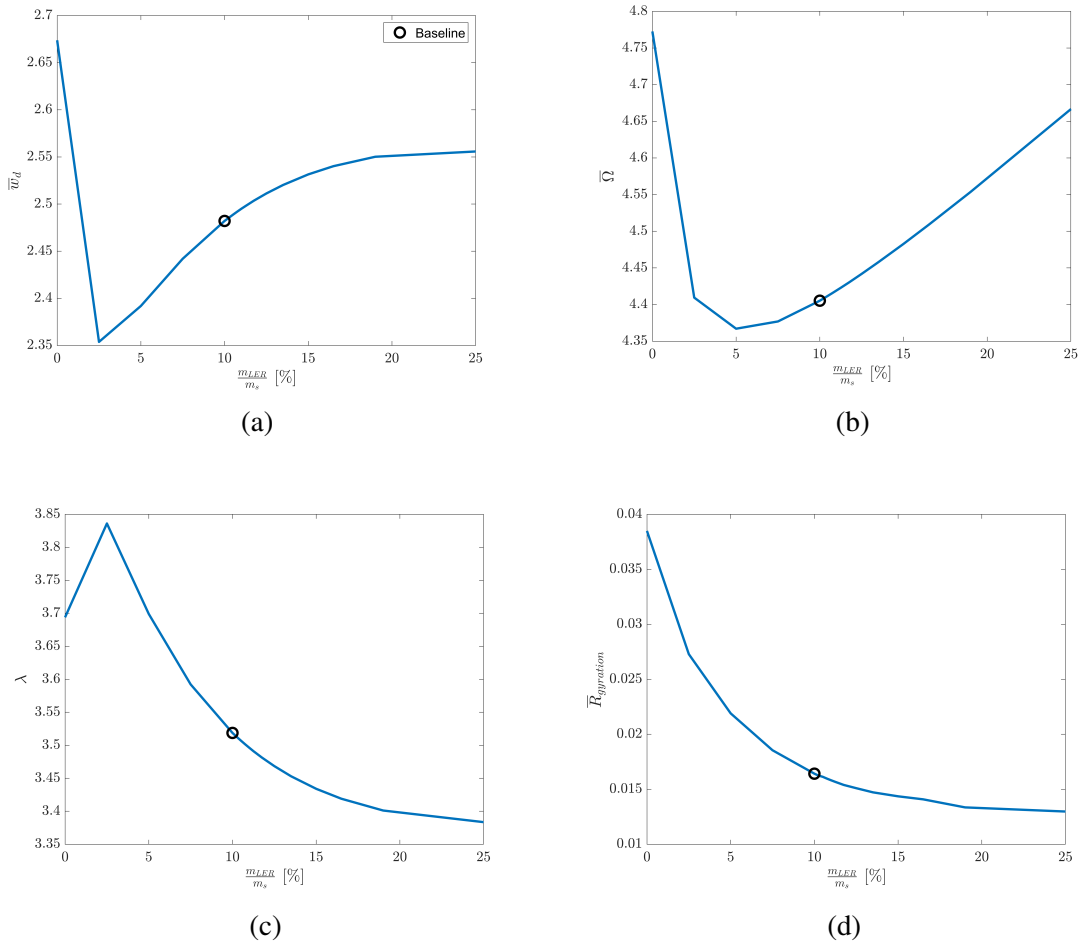

Fig. 3.10. Steady average values of variables of motion as LER mass is varied. (a) Vertical descent velocity w_d. Subfigure (b) Angular velocity Ω . (c) tip speed ratio λ. (d) Radius of gyration

It is important to remark that for continuously increasing rod mass no unstable autorotation was found until rod mass values of around (50% $\overline{m}_s$), where samara was not able to achieve autorotation motion.

Regarding the center of gravity, as represented in figure 3.12, displacement of center of gravity behaves linearly which is consequent of its definition $\boldsymbol{x}_{CG} = \frac{\sum \boldsymbol{x}_i m_i}{\sum m_i}$. A logical trend is observed, the position of the center of gravity displaces towards the LE in the chordal direction while in the spanwise, center of gravity is translated positively as rod mass increases.

Due to the nature of the analysis, as previously, inertia is varied linearly. By definition, $I \propto mr^2$, so that inertia will vary linearly with the mass as the position vector of each vector is not changed. This behaviour of inertia is exemplified in figures 3.13. Globally all components of inertia will grow as rod mass does the same and vice-versa. As a consequence of the bigger inertia contribution variation of the rod than the one of the nut. However, it is distinguishable that $\overline{I}_x$ and $\overline{I}_z$ will be higher varied than $\overline{I}_z$, while the cross product of inertia $\overline{I}_{xy}$ will the most affected one. Cross product is much altered ranging

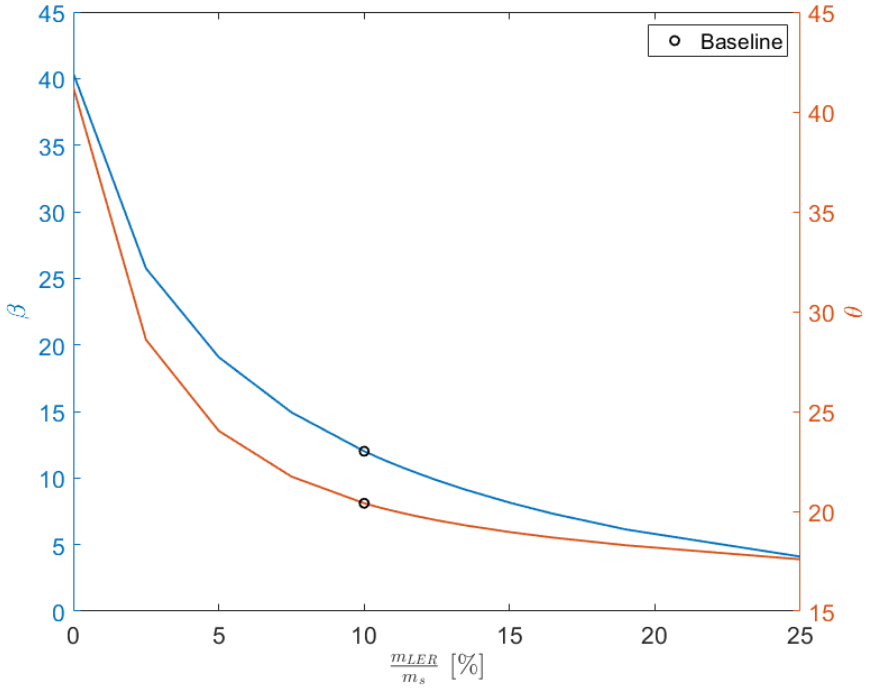

Fig. 3.11. Flight angles as LER mass is varied: (—) β; (—) θ

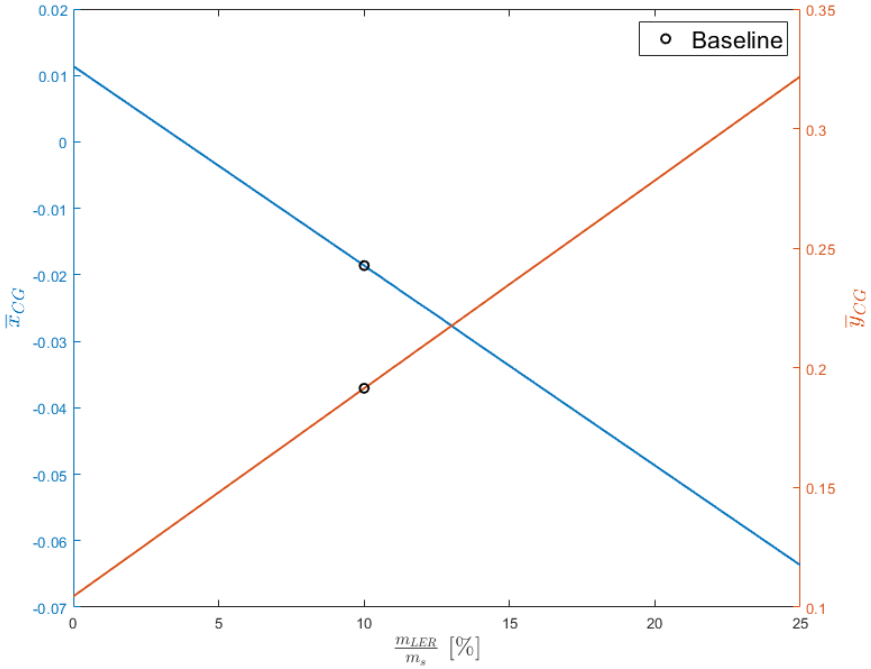

Fig. 3.12. Seed's gravity center with respect to $\sum_C$ as rod mass is varied: (—) $\overline{x}_{CG}$; (—) $\overline{y}_{CG}$

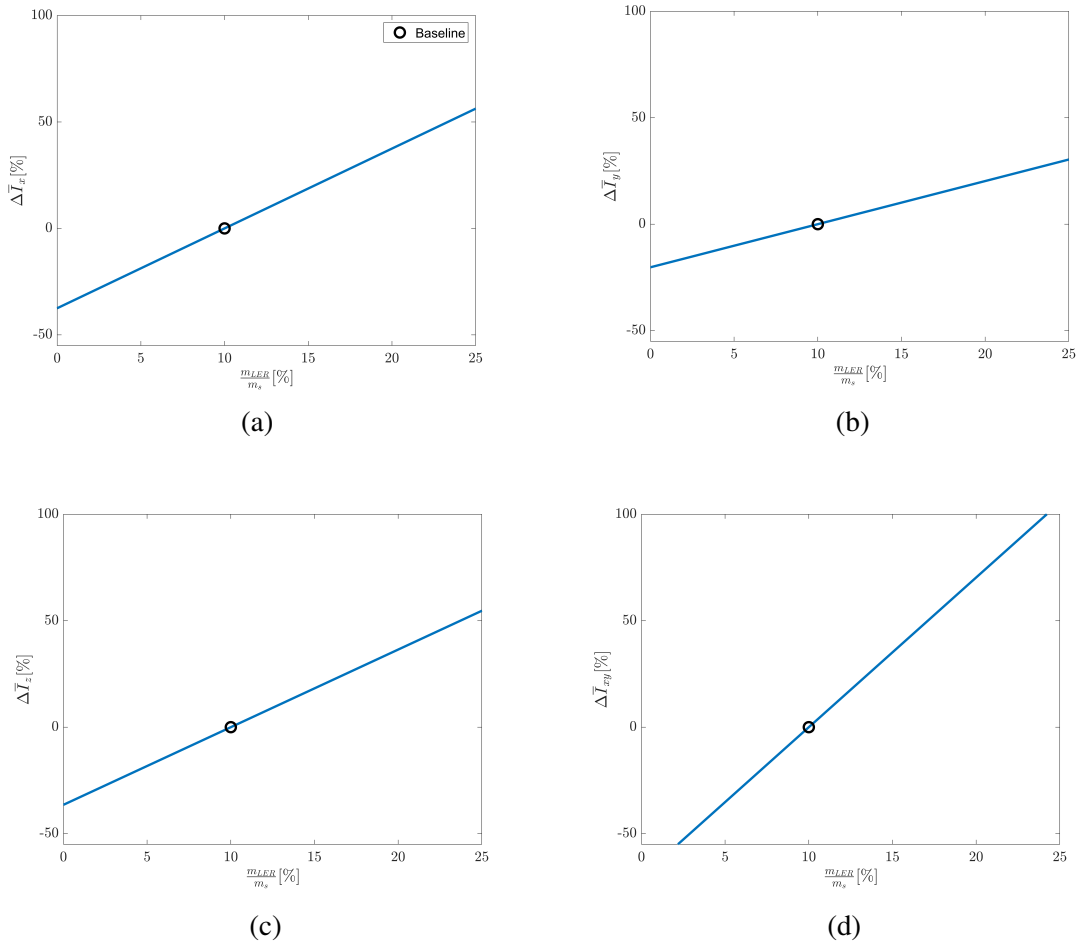

Fig. 3.13. Change percentage of the tensor of inertia with respect to its original position as LER mass is varied. Inertia is computed with respect to nut center $\sum_C$. (a) Inertia in axis x_C. (b) Inertia in axis y_C. (c) Inertia in axis z_C. (d) Cross product of inertia xy_C

from -50% to 100% of the original values as will *sum* contribution of displacements in both x and y directions.

Furthermore, the relative huge variations of cross product of inertia are translated, when solving the corresponding eigenvalue problem, in a considerable variation of the angle formed by the principal directions of inertia. Figure 3.14 displayed remarkably how angle increases as rod mass does the same. This result coincides with previous sections. It suggests a huge contribution over autorotation as a coupling mechanism of both directions. Moreover, optimal motion is found in both parametric studies around a value of 6º of the principals directions for the geometrical model employed.

From the point of view of seed's trajectory, seed with no LER did not exhibited considerable horizontal displacement apart from the initial transient as it can be seen in figure 3.15. As the rod mass increments, higher horizontal displacements are observed, with higher radius of translation. For the last simulation performed, $\overline{m}_{LE} = 25\% \, \overline{m}_s$, trajectory exhibited a different behaviour in which seed experienced a large transient with large displacement in the original transient direction, then seed returning to the initial point until

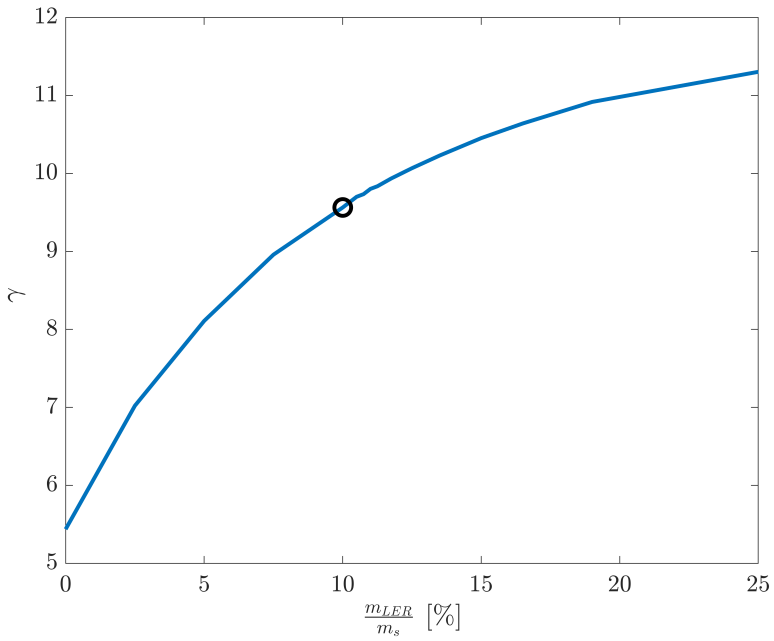

Fig. 3.14. Angle between principal directions of inertia and $\sum_B$ as LER mass is varied

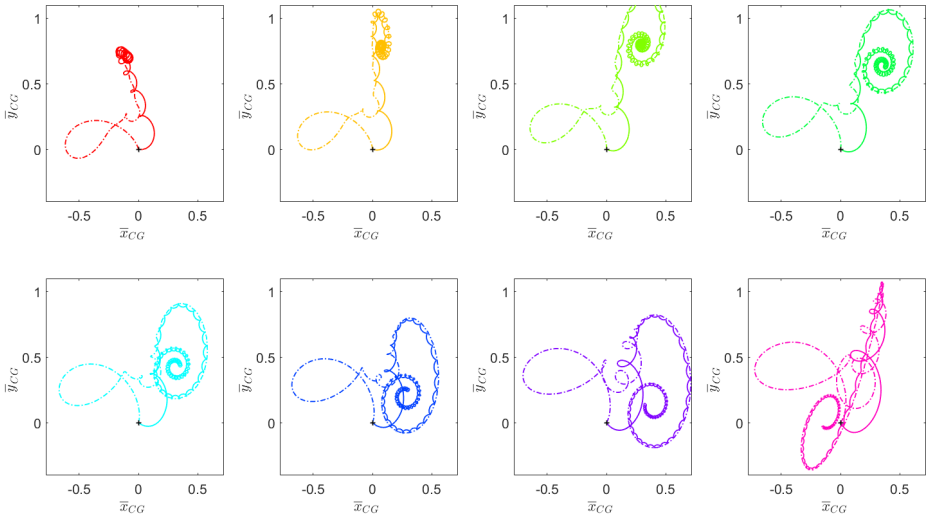

Fig. 3.15. Trajectories of seed's center of gravity as LER mass is varied together with their ICRs. (—) no LE. (—) $\overline{m}_{LE} = 2.5\%\,\overline{m}_s$. (—) $\overline{m}_{LE} = 7.5\%\,\overline{m}_s$. (—) $\overline{m}_{LE} = 10\%\,\overline{m}_s$. (—) $\overline{m}_{LE} = 12.5\%\,\overline{m}_s$. (—) $\overline{m}_{LE} = 15\%\,\overline{m}_s$. (—) $\overline{m}_{LE} = 19\%\,\overline{m}_s$. (—) $\overline{m}_{LE} = 25\%\,\overline{m}_s$

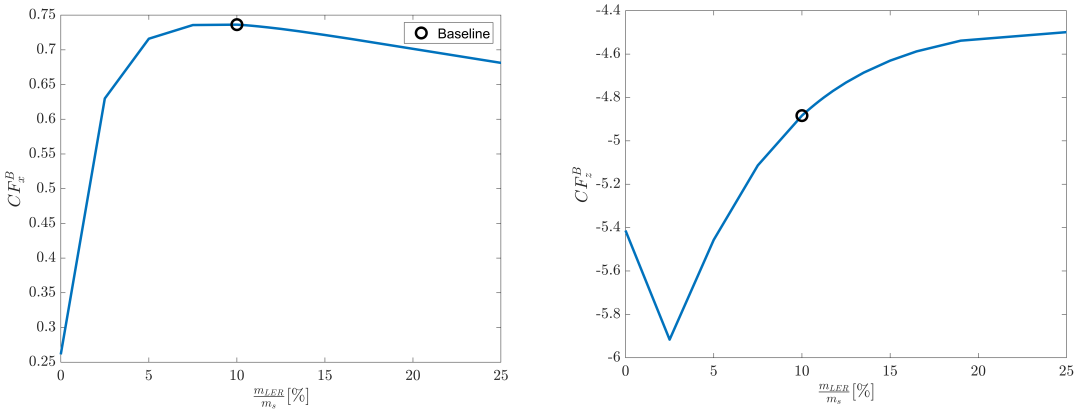

(a) (b)

Fig. 3.16. Aerodynamic forces in $\sum_B$ as LER mass is varied. (a) x_B component. (b) z_B component

stable autorotation is reached.

Regarding the aerodynamic forces, the same force coefficients are used as displayed in figure 3.16. From figure 3.16a, it can be inferred that the higher change in CF_x^B is produced as rod mass is increased from a null value up to around 3% of the total seed mass. Consequently, as it displayed in figure 3.15, this is translated into a reduced displacement of seed in the horizontal plane. For CF_z^B trend will be different, it reaches a minimum which therefore descent velocity will reach a maximum. However, as rod mass continues to increase and tends to stabilize, descent velocity will do the same.

For the case of moments, CM_x^B and CM_z^B will have a small initial increase while reaching the minimum at 2.5% $\overline{m}_s$ where moments will tend to decrease. However, CM_z^B displayed a parabolic shape with a minimum at around 6.5% $\overline{m}_s$ and tending do decrease slightly as rod mass increases.

It can be concluded, after analysis of main variables, that an optimal samara autorotation interval was found $\overline{m}_{LER} \in [2.5\ 10]\ \%m_s$ for the developed geometrical model. Samara autorotation performance is enhanced in the interval. For lower values of rod mass, the samara experienced higher descent velocity, translating lower in the horizontal plane while spinning faster. However, for higher values, the seed descended at higher velocities, spinning faster, lower radius of gyration but with higher displacement in the horizontal plane. Moreover, from values of 15%$\overline{m}_s$ on, many variables of motion tended to be constant, showing insensitivity up to very values as it can be seen in trajectory for $\overline{m}_{LE} = 25\%\ \overline{m}_s$.

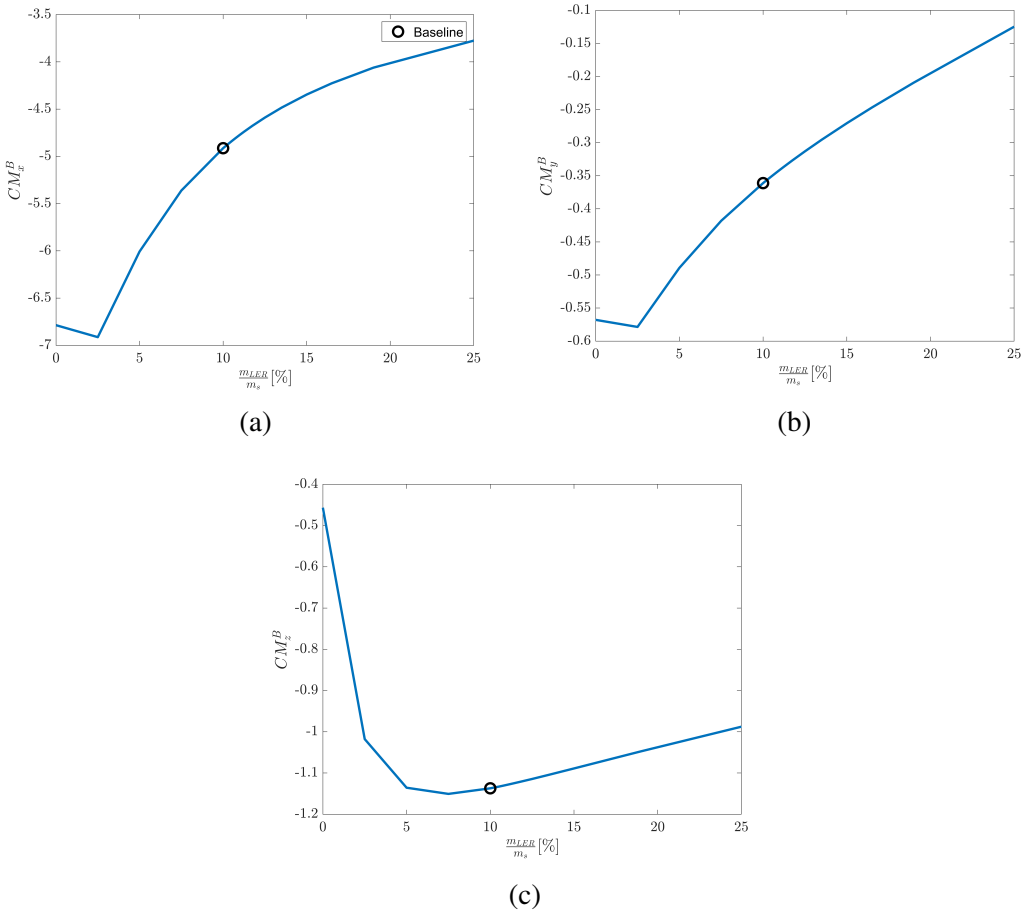

Fig. 3.17. Aerodynamic forces in $\sum_B$ as LE mass is varied. (a) x_B component. (b) y_B component. (c) z_B component

4. CONCLUSION AND FUTURE WORK

This chapter gathers the conclusions extracted from the thesis and future line of improvements.

4.1. Conclusion

The numerical model presented in the thesis was developed and different parametric studies of inertia properties of seeds in autorotation have been performed. Studies have revealed relevant inertia insights that few still need to be proven accordingly. Nevertheless, the main objective of the thesis can be considered fully accomplished.

First, it was observed the good agreement between the numerical model developed and the empirical data, considering the simplistic model developed in the project. The numerical model has a considerable number of assumptions: aerodynamics coefficients, two-dimensional flow over blade element neglecting spanwise forces, the velocity constant over the blade (u_i) and seed's planar model, including others. Nevertheless, results have proven to be encouraging. Moreover, the numerical model was intended to be used to obtain general trends of inertia effects instead of providing exact results, which might be provided more accurately by DNS methods.

Secondly, addressing inertia properties is a complex non-straight problem. In order to do so, it was thought to imposed different inertia tensor and try to resolve the inverse problem and obtain the geometry that would provide such inertia. Yet, the inverting process is not straight and might lead to non-singularities: unrealistic cases, multiple geometries or any solution. Therefore parametric studies were performed isolating inertia contribution by preserving the same aerodynamic module (same wing) and same weight (seed's mass). Therefore, two parametric studies were performed according to these criteria. First, LER was displaced in a rectangular domain. Second, seed's mass distribution was altered by tuning LER and nut mass. In both cases, inertia properties and samara's center of gravity are modified.

On one hand, modifying LER position has shown that x_L was the more sensible direction. An unstable frontier was reached at a value closed to the one predicted by Norberg (1973). The slope in level contour might be due to the coupling on both directions. This coupling is more evident when analysing flight angles as both tend to converge to same values when approaching the frontier. Most important insight regarding this coupling is found in the angle between $\sum_B$ and $\sum_P$ contour, unstable frontier fell exactly following an angle level. It suggests the huge contribution of the principal directions on this coupling and on the autorotation motion in general. Additionally, different trajectories were represented to display the effect on moving on both directions, while displacing LER in x_L, the seed will experience a larger horizontal displacement before reaching autorotation.

Displacing LER in y_L entails higher radius of translation of seed's center. Additionally, seed's center of gravity has proven to influence greatly seed's stability.

On the other hand, modifying LER mass has shown variables of motion trends. It was found that there is an LER mass interval of $m_{LER} \in [2-5]\%m_s$ where variables are optimized. In the interval, the seed will minimize their descent speed while maximizing its spinning rate. This motion will be beneficial to samara seed as a higher time to fall as well as a quick change of orientation of seed (spinning) will help the seed to be carried away by a wind gust. The author believes that real samaras will be naturally designed in that interval, nevertheless, it needs to be proven empirically. Additionally, as previously, the angle formed by principals direction exhibited similar contribution, optimal values for principal directions angle around 6^o was found, which is similar to the optimal of previous analysis. Additionally, trajectories were specially altered for small values of LER mass, while showing almost insensitivity until very high values. The radius of rotation of seed's gravity center increases as LER mass does the same.

All in all, although the problem is complex due to coupling reasons, best effort to elucidate inertia effect was performed obtaining relevant insights. Nevertheless, there are still things to be investigated in order to completely understand the inertia effects and therefore it is proposed as further work.

4.2. Future work

Although results have been satisfactory, and the main objective has been accomplished, the study of inertia effects should be extended to better understand it. Several lines of improvements are distinguished.

First of all, numerical model improvements might be envisaged. It might incorporate tip speed corrections as Glauert (1935), spanwise velocity component as Rosen and Seter (1991), include aerodynamic contribution of nut and ribs (corrugated wing)... These improvements would surely make the numerical model more accurate. Nevertheless, the main limitation of BEM will constitute the assumption of the aerodynamic coefficients, difficult to measure experimentally in such small wings and Reynolds numbers.

Secondly, other parametric studies can be performed to increase inertia properties knowledge on autorotation. In order to do so, the author believes that inertia properties must be completely isolated to be studied. Therefore, the center of gravity must be fixed artificially while inertia properties are modified, especially focusing on the angle of principals direction or the cross product of inertia. For example, it is proposed as further work to recreate the contours by imposing inertia properties of each grid point while preserving the same center of gravity in order to assess the contribution of inertia and center of gravity for stability.Another possible line might be a parametric study consisting of the modification of the angle of principal directions artificially.

Moreover, other research lines might be to check the trends of the results, obtained

in the project by DNS. In this fashion, the result obtained would be double-checked and would allow to research the effect of inertia for example on the LEV, of vital importance as found in Lentink et al. (2009).

BIBLIOGRAPHY

Anderson Jr, J. D.
2010. Fundamental of aerodynamics [si units].

Arranz, G., A. Gonzalo, M. Uhlmann, O. Flores, and M. García-Villalba
2018a. A numerical study of the flow around a model winged seed in auto-rotation. *Flow, Turbulence and Combustion*, 101(2):477–497.

Arranz, G., M. Moriche, M. Uhlmann, O. Flores, and M. Garcia-Villalba
2018b. Kinematics and dynamics of the auto-rotation of a model winged seed. *Bioinspiration & biomimetics*, 13(3):036011.

Augspurger, C. K.
1986. Morphology and dispersal potential of wind-dispersed diaspores of neotropical trees. *American journal of Botany*, 73(3):353–363.

Azuma, A.
1981. An extension of the local momentum theory to the rotors operating in the twisted flow field. In *Proc. 7th Europ. Rotorcr. Power LiftAircr. Forum*, volume 5, Pp. 1–18.

Azuma, A.
2006. *The biokinetics of flying and swimming*. American Institute of Aeronautics and Astronautics.

Azuma, A. and K. Yasuda
1989. Flight performance of rotary seeds. *Journal of Theoretical Biology*, 138(1):23–53.

Birch, J. M. and M. H. Dickinson
2001. Spanwise flow and the attachment of the leading-edge vortex on insect wings. *Nature*, 412(6848):729.

Burke, J. D.
1989. Atmospheric autorotating imaging device. US Patent 4,886,222.

Burrows, F.
1975. Wind-borne seed and fruit movement. *New phytologist*, 75(2):405–418.

Crimi, P.
1988. Analysis of samara-wing decelerator steady-state characteristics. *Journal of Aircraft*, 25(1):41–47.

Dickinson, M. H. and K. G. Gotz
1993. Unsteady aerodynamic performance of model wings at low reynolds numbers. *Journal of Experimental Biology*, 174(1):45–64.

Fregene, K., D. Sharp, C. Bolden, J. King, C. Stoneking, and S. Jameson
2011. Autonomous guidance and control of a biomimetic single-wing mav. In *AUVSI Unmanned Systems Conference*, Pp. 1–12. Assoc. for Unmanned Vehicle Systems International Arlington, VA.

Ginsberg, J.
2008. *Engineering dynamics*, volume 10. Cambridge University Press.

Glauert, H.
1935. Airplane propellers. In *Aerodynamic theory*, Pp. 169–360. Springer.

Green, D. S.
1980. The terminal velocity and dispersal of spinning samaras. *American Journal of Botany*, 67(8):1218–1224.

Jameson, S., K. Fregene, M. Chang, N. Allen, H. Youngren, and J. Scroggins
2012. Lockheed martin's samarai nano air vehicle: challenges, research, and realization. In *50th AIAA Aerospace Sciences Meeting Including the New Horizons Forum and Aerospace Exposition*, P. 584.

Jameson, S., B. Satterfield, C. Bolden, N. Allen, C. Palmdale, H. Youngren, and M. Portland
2007. Samarai nano air vehicle-a revolution in flight. *DARPA contract W31P4Q-06-C-0324*.

Jenkins, D. and B. Vasigh
2013. *The economic impact of unmanned aircraft systems integration in the United States*. Association for Unmanned Vehicle Systems International (AUVSI).

Kroo, I.
1995. Single-winged autorotating brake for sensor deployment on mars.

Lee, I.
2016. *Numerical study of a freely-falling maple seed*. PhD thesis, Seoul National University.

Lee, S. J., E. J. Lee, and M. H. Sohn
2014. Mechanism of autorotation flight of maple samaras (acer palmatum). *Experiments in fluids*, 55(4):1718.

Lentink, D., W. B. Dickson, J. L. Van Leeuwen, and M. H. Dickinson
2009. Leading-edge vortices elevate lift of autorotating plant seeds. *Science*, 324(5933):1438–1440.

LeVeque, R. J.
2007. *Finite difference methods for ordinary and partial differential equations: steady-state and time-dependent problems*, volume 98. Siam.

Marsden, J. E. and A. Tromba
2003. *Vector calculus*. Macmillan.

Maxwell, J. C.
1854. On a particular case of the descent of a heavy body in a resisting medium. *Camb. Dublin Math. J*, 9:145–148.

Nathan, R.
2006. Long-distance dispersal of plants. *Science*, 313(5788):786–788.

Norberg, R. Å.
1973. Autorotation, self-stability, and structure of single-winged fruits and seeds (samaras) with comparative remarks on animal flight. *Biological Reviews*, 48(4):561–596.

Pounds, P. and S. Singh
2015. Samara: Biologically inspired self-deploying sensor networks. *IEEE Potentials*, 34(2):10–14.

Rao, M., D. C. Hoysall, and J. Gopalan
2014. Mahogany seed–a step forward in deciphering autorotation. *Current Science*, 106(8):1101.

Roccia, B., S. Preidikman, L. Ceballos, and J. Massa
2014. Estudio de la aerodinámica no lineal e inestacionaria de semillas voladoras autorrotantes. *Mecánica Comptacional*, 33(18).

Rosen, A. and D. Seter
1991. Vertical autorotation of a single-winged samara. *Journal of applied mechanics*, 58(4):1064–1071.

Salcedo, E. and R. O. Vargas
2013. Stereoscopic particle image velocimetry measurements of the three-dimensional flow field of a descending autorotating mahogany seed (swietenia macrophylla). *Journal of Experimental Biology*, 216(11):2017–2030.

Seter, D. and A. Rosen
1992a. Stability of the vertical autorotation of a single-winged samara. *Journal of applied mechanics*, 59(4):1000–1008.

Seter, D. and A. Rosen
1992b. Study of the vertical autorotation of a singlewinged samara. *Biological Reviews*, 67(2):175–197.

Tewari, A.
2007. *Atmospheric and space flight dynamics*. Springer.

Ulrich, E. R., D. J. Pines, and J. S. Humbert
2010. From falling to flying: the path to powered flight of a robotic samara nano air vehicle. *Bioinspiration & biomimetics*, 5(4):045009.

Varshney, K., S. Chang, and Z. J. Wang
2011. The kinematics of falling maple seeds and the initial transition to a helical motion. *Nonlinearity*, 25(1):C1.

Yasuda, K. and A. Azuma
1997. The autorotation boundary in the flight of samaras. *Journal of Theoretical Biology*, 185(3):313–320.

Appendices

A. INERTIA PROPERTIES

In this appendix, all computations regarding the inertia properties of the seed model are presented. Moment of inertia of seed can be difficult a priori to compute, in order to properly address it, samara seed was separated in different pieces summing their contributions.

Inertia properties are initially calculated in $\sum_N$ body reference frame centered at the nut. One should notice that $\sum_N$ corresponds to the same reference frame as $\sum_C$. Then inertia was properly displaced to the seed gravity center using *Steiner's theorem*.

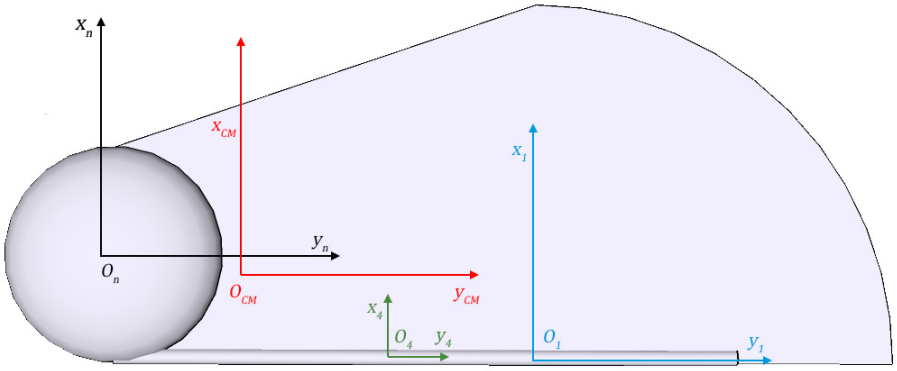

Fig. A.1. Representation of different body reference frame used for inertia computations

A.1. Center of nut

A.1.1. Nut

The nut was modeled as an oblate ellipsoid which properties are ready known (Ginsberg, 2008).

$$I^N_{x_{nut}} = \frac{1}{5}m_n(r_n^2 + h_n^2) \qquad I^N_{y_{nut}} = \frac{1}{5}m_n(r_n^2 + h_n^2) \qquad I^N_{z_{nut}} = \frac{2}{5}m_n r_n^2 \tag{A.1}$$

A.1.2. Wing

The seed wing will require more computations. Samara wing was divided in two main parts: a quarter of circle (A1) and a trapezoid without cylinder (A2) .

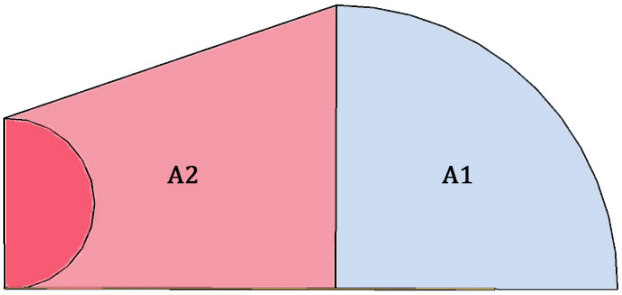

Fig. A.2. Representation of the wing areas

A quarter of a circle is also quite easily obtained from bibliography but in this report was computed by hand.

For convenience, Area 1 inertia was computed with respect to $\sum_1$ which is a body parallel reference frame but attached to the nut center, as it is displayed in figure A.1.

$$I^1_{x_{A1}} = \iiint (y^2 + z^2)\, dm \qquad I^1_{y_{A1}} = \iiint (x^2 + z^2)\, dm \qquad I^1_{z_{A1}} = \iiint (x^2 + y^2)\, dm \tag{A.2}$$

where $dm = rho_w\, dxdydz$

For the proper resolution of integrals A.2, transformation of coordinates was performed from cartesian to polar.

$$x = r\cos(x) \tag{A.3}$$

$$y = r\sin(y) \tag{A.4}$$

Recalling from vector calculus (for further references Marsden and Tromba (2003))

$$\iiint f(x,y,z)dxdydz = \iiint f(r,\theta,z)\left|\frac{\partial(x,y,z)}{\partial(r,\theta,z)}\right| drd\theta dz \tag{A.5}$$

Thus deriving in

$$\iiint f(x,y,z)\, dxdydz = \iiint f(r,\theta,z)\, r\, drd\theta dz \tag{A.6}$$

As each inertia integral is composed by the sum of two components. Integrals will be split into them and then sum them in order to avoid repetition.

$$\iiint_{A1} x^2\, dxdydz = \int_{-\frac{t}{2}}^{\frac{t}{2}} \int_0^{\frac{\pi}{2}} \int_0^c r^3 \sin^2(x)\, drd\theta dz = \frac{\pi c^4 t}{16} \tag{A.7}$$

Integral of y^2 yields the same result as a consequence of parity?

$$\iiint_{A1} y^2\, dxdydz = \int_{-\frac{t}{2}}^{\frac{t}{2}} \int_0^{\frac{\pi}{2}} \int_0^c r^3 \cos^2(x)\, drd\theta dz = \frac{\pi c^4 t}{16} \tag{A.8}$$

$$\iiint_{A1} z^2\, dxdydz = \int_{-\frac{t}{2}}^{\frac{t}{2}} \int_0^{\frac{\pi}{2}} \int_0^c z^2 r\, drd\theta dz = \frac{A_1 t^3}{12} = \frac{\pi c^2 t^3}{48} \tag{A.9}$$

Therefore the moments of inertia in each axis, summing each contribution, results in:

$$I^1_{x_{A1}} = I^1_{y_{A1}} = \rho_w \left(\frac{a^4 \pi t}{16} + \frac{A_1 t^3}{12} \right) = \rho_w \frac{\pi c^2 t}{16} \left(\frac{t^2}{3} + c^2 \right) \tag{A.10}$$

$$I^1_{z_{A1}} = \rho_w \frac{\pi c^4 t}{8} \tag{A.11}$$

The cross products of inertia will be computed in a similar way. Cross products of inertia of axis z will be null due to symmetry principles and I_{xy} will be

$$I^1_{xy_{A1}} = \iiint_{A1} xy\, dxdydz = \int_{-\frac{t}{2}}^{\frac{t}{2}} \int_0^{\frac{\pi}{2}} \int_0^c \rho_w r^3 \cos(x) \sin(x)\, drd\theta dz = \rho_w \frac{c^4 t}{8} \tag{A.12}$$

$$\bar{\bar{I}}^1_{A1} = \begin{pmatrix} I_{x_1} & I_{xy_1} & 0 \\ I_{xy_1} & I_{y_1} & 0 \\ 0 & 0 & I_{z_1} \end{pmatrix}$$

The moments of inertia of Area 1 must be translated to the nut center with the aid of *Steiner's theorem*. However, *Steiner's theorem* only relates the inertia properties of center of mass of the area with an arbitrary one. So inertia of Area 1 cannot be translated directly to nut center nor seed's gravity center. So the previously computed inertia has to be displaced from $O_1 x_1 y_1$ to the center of mass of Area 1 and then wherever is wanted.

By geometry principles, it is known that the quarter of circle centroid is

$$\vec{r}_{O_1 c_{A1}} = \left[\frac{4c}{3\pi}, \frac{4c}{3\pi}, 0 \right]^T \tag{A.13}$$

Applying *Steiner's theorem*

$$\bar{\bar{I}}^{c_{A1}}_{A1} = \bar{\bar{I}}^1_{A1} - m_{A1} \left(r^2_{O_1 c_{A1}} \bar{\bar{U}} - [\boldsymbol{r_{O_1 c_{A1}}} \boldsymbol{r_{O_1 c_{A1}}}] \right) \tag{A.14}$$

Then inertia is computed at the center of the nut as

$$\bar{\bar{I}}^N_{A1} = \bar{\bar{I}}^{c_{A1}}_{A1} - m_{A1} \left(r^2_{O_n c_{A1}} \bar{\bar{U}} - [\boldsymbol{r_{O_n c_{A1}}} \boldsymbol{r_{O_n c_{A1}}}] \right) \tag{A.15}$$

where $r_{O_n c_{A1}}$ is the vector position that goes from the nut center to Area 1 centroid.

Now the inertia properties of Area 2 is going to be presented. In this case integrals of inertia were performed with respect to the center of the nut. The difficulty here resides on the geometry of Area 2, which is a trapezoid to which half of circle is subtracted (half nut platform) as displayed in A.2. The way to proceed will be to integrate the trapezoid area and then subtract the inertia corresponding to the semicircle.

$$\iiint_{A_{trap}} x^2\, dxdydz = \int_{-\frac{t}{2}}^{\frac{t}{2}} \int_0^{y^*} \int_{-r_n}^{r_n + \frac{h}{y^*} y} x^2\, dxdydz = \frac{y^* t}{12} (8r_n^3 + 6r_n^2 h + 4r_n h^2 + h^3) \tag{A.16}$$

$$\iiint_{A_{trap}} y^2\,dxdydz = \int_{-\frac{t}{2}}^{\frac{t}{2}} \int_0^{y^*} \int_{-r_n}^{r_n+\frac{h}{y^*}} x^2\,dxdydz = \frac{y^{*3}t}{12}(8r_n + 3h) \tag{A.17}$$

$$\iiint_{A_{trap}} z^2\,dxdydz = \int_{-\frac{t}{2}}^{\frac{t}{2}} \int_0^{y^*} \int_{-r_n}^{r_n+\frac{h}{y^*}} z^2\,dxdydz = \frac{y^* t^3}{24}(4r_n + h) \tag{A.18}$$

$$\iiint_{A_{trap}} xy\,dxdydz = \int_{-\frac{t}{2}}^{\frac{t}{2}} \int_0^{y^*} \int_{-r_n}^{r_n+\frac{h}{y^*}} xy\,dxdydz = \frac{y^* h t^3}{24}(8r_n + 3h) \tag{A.19}$$

Integrals of semicircle are solved together

$$\begin{aligned} Int_{x_c} &= \iiint_{A_{semicircle}} (y^2 + z^2)\,dxdydz = \int_{\frac{-t}{2}}^{\frac{t}{2}} \int_0^{r_n} \int_0^{\pi} = (r^3 \sin^2\theta + z^2 r)\,d\theta dr dz \\ &= \frac{\pi r_n^4 t}{8} + \frac{A_3}{2}\left(\frac{t^3}{12}\right) = \frac{\pi r_n^2 t}{8}\left(r_n^2 + \frac{t^3}{3}\right) \end{aligned} \tag{A.20}$$

For the y axis, the integral will end in the same result

$$Int_{y_c} = \int_{\frac{-t}{2}}^{\frac{t}{2}} \int_0^{r_n} \int_0^{\pi} (r^3 \cos^2\theta + z^2 r)\,d\theta dr dz = \frac{\pi r_n^4 t}{8} + \frac{A_3}{2}\left(\frac{t^3}{12}\right) = \frac{\pi r_n^2 t}{8}\left(r_n^2 + \frac{t^3}{3}\right) \tag{A.21}$$

$$Int_{z_c} = \iiint_{A_{semicircle}} (x^2 + y^2)\,dxdydz = \int_{\frac{-t}{2}}^{\frac{t}{2}} \int_0^{r_n} \int_0^{\pi} = r^3\,d\theta dr dz = \frac{\pi r_n^4 t}{4} \tag{A.22}$$

Cross product of inertia are null due to symmetry around y axis

$$Int_{xy_c} = \iiint_{A_{semicircle}} xy\,dxdydz = \int_{\frac{-t}{2}}^{\frac{t}{2}} \int_0^{r_n} \int_0^{\pi} r^3 \sin\theta\cos\theta\,d\theta dr dz = 0 \tag{A.23}$$

As both inertias are computed directly from the nut center, inertia of the resulting Area 2 just consist of the one of the trapezoid subtracting the semicircle area as

$$I^N_{x_{A2}} = \rho_w\left(Int_{y^2} + Int_{z^2} - I_{x_c}\right) \tag{A.24}$$

$$I^N_{y_{A2}} = \rho_w\left(Int_{x^2} + Int_{z^2} - I_{y_c}\right) \tag{A.25}$$

$$I^N_{z_{A2}} = \rho_w\left(Int_{x^2} + Int_{y^2} - I_{z_c}\right) \tag{A.26}$$

$$I^N_{xy_{A2}} = \rho_w\left(Int_{xy}\right) \tag{A.27}$$

So the inertia wing properties will be given by the superposition principle summing each area contribution

$$\overline{\overline{I_w}}^N = \overline{\overline{I_{A1}}}^N + \overline{\overline{I_{A2}}}^N \tag{A.28}$$

A.1.3. Leading Edge Rod

Leading Edge Rod was modeled as a long and thin cylinder. Inertias properties are easily computable but it was not performed as the mathematical development does not provide any relevant insights. So they were taken from Ginsberg (2008). Inertial was taken with respect to its own center of mass. Furthermore, due to accuracy reasonings, that may arise when increasing diameter size, inertia properties were chosen to be the one corresponding to a normal cylinder instead of using thin cylinder approximation, by which the inertia across its longitudinal axis is assumed to be negligible. Therefore the rod inertia properties were

$$I_x^4 = I_z^4 = \frac{m_{LER}}{48}\left(3D_{LER}^2 + 4b^2\right) \tag{A.29}$$

$$I_y^4 = \frac{m_{LER}}{8}D_{LER}^2 \tag{A.30}$$

Now LER has to be properly displaced to the center of the nut by using again *Steiner's theorem*.

$$\overline{\overline{I}}_{LER}^{N} = \overline{\overline{I}}_{LER}^{4} + m_{LER}\left(r_{O_N O_4}^2\overline{\overline{U}} - [\boldsymbol{r_{O_N O_4}}\boldsymbol{r_{O_N O_4}}]\right) \tag{A.31}$$

where $r_{O_N O_4}$ will be the vector position that goes from the center of the nut to the rod center of gravity.

A.2. Center of mass

The previous computed moments of inertia have to be carefully displaced to the seed's gravity center, computed in section 2.2.2, taking into consideration the additional area reference frames from where its part inertia has been computed.

Nut moments of inertia are obtained following a straightforward application of *Steiner's theorem*.

$$\overline{\overline{I}}_{Nut}^{CM} = \overline{\overline{I}}_{Nut}^{N} + m_{Nut}\left(r_{CM}^2\overline{\overline{U}} - [\boldsymbol{r_{CM}}\boldsymbol{r_{CM}}]\right) \tag{A.32}$$

Wing inertia is displaced by displacing each area separately. For Area 1 inertia has to be displaced from its centroid so that Steiner can be applied. It is important to remember that Area 1 centered with respect to $O_1 x_1 y_x 1$ is given by A.13 . So the vector position of Area 1 centroid w.r.t $\sum_{CM}$ will be given as

$$\vec{r}_{CM\,C_1} = \vec{r}_{CM\,O_N} + \vec{r}_{O_N\,O_1} + \vec{r}_{O_1\,C_1} \tag{A.33}$$

$$\overline{\overline{I}}_{A1}^{CM} = \overline{\overline{I}}_{A1}^{C1} + m_1\left(r_{CM\,C_1}^2\overline{\overline{U}} - [\boldsymbol{r_{CM\,C_1}}\boldsymbol{r_{CM\,C_1}}]\right) \tag{A.34}$$

In area 2, the procedure is more troublesome as the integrals of inertia were computed with respect to $\sum_N$. Therefore by geometrical principals, area 2 centroid position was calculated by first computing the trapezoid centroid and then by proportionality of area, Area 2 centroid was located. Once Area2 centroid was located, *Steiner's* was once again applied.

$$\bar{\bar{I}}_{A2}^{CM} = \bar{\bar{I}}_{A2}^{C2} + m_{A2}\left(r_{CM\,C_2}^2\,\bar{\bar{U}} - [\boldsymbol{r_{CM\,C_2}}\boldsymbol{r_{CM\,C_2}}]\right) \tag{A.35}$$

Lastly LE rod inertia will be translated as

$$\bar{\bar{I}}_{LER}^{CM} = \bar{\bar{I}}_{LER}^{4} + m_{LER}\left(r_{CM\,O_4}^2\,\bar{\bar{U}} - [\boldsymbol{r_{CM\,O_4}}\boldsymbol{r_{CM\,O_4}}]\right) \tag{A.36}$$

B. BUDGET PROJECT AND PLANNING

This appendix details the project planning carried for the satisfactory development of the current thesis, tasks breakdown and schedule is presented in section B.1. In addition, an estimation of the budget required is given making difference by type of costs, see B.2

B.1. Planning

Thesis started, as in any other considerable size project, by definition of the project. Although small time was devoted to this task, this preliminary one is vital as it is the pillar upon which the project was built, everything must be clear at that point before starting to work. Definition of the project was mainly performed with my supervisor who made recommendations and finally approved the intended project.

Secondly, the code development took most of the time, everything defined had to be properly coded and everything was started from scratch. Furthermore, once code was almost completely finished, validation and comparison of data with bibliography have to be performed. This task consist of a feedback activity which errors of codes were found and analysis of results performed. Once finished, the representation code had to be implemented.

Finally, thesis writing was the second most time-consuming task, everything interesting had to be presented in an understandable way and important insights must be highlighted from lesser important ones.

All in all, project planning by activity and date is summarised in table B.1. Moreover, *Gantt* diagram B.1 provides a visual representation of task accomplishment during the thesis duration.

ID	Starting Date	Ending date	Task
1	01/09/2018	15/09/2018	Project definition
1.1			Bibliographic research
1.2			Objectives
1.3			Geometrical model
1.4			Equations of motion/ref. frame
1.5			Numerical method selection
2	15/09/2018	02/03/2019	Matlab coding
2.1			Geometry computations
2.2			Samara discretization
2.3			Definition of reference frames and rotations
2.4			Aerodynamic module
2.5			Numerical schema implementation
2.6			Results representation
3	25/01/2019	02/03/2019	Validation & analysis of results
4	28/02/2019	31/05/2019	Thesis writing

Table B.1. Task planning and accomplished

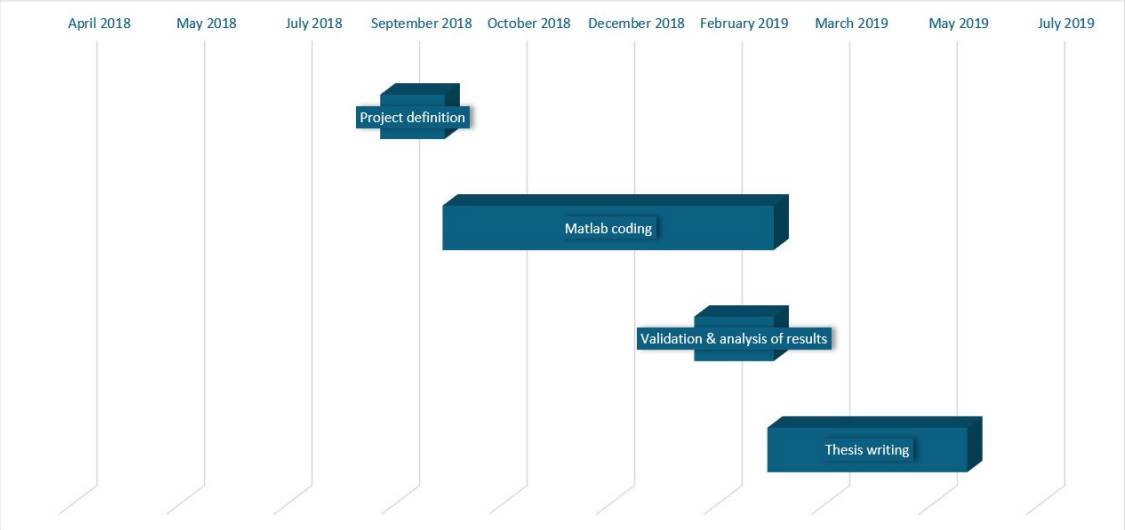

Fig. B.1. Gantt project diagram

B.2. Budget

In this section, an overall estimated budget is developed. It is important to remark that this just consists of estimation as variables as electricity costs student salary may be relative or may fluctuate. However main interest here will reside on providing an estimation of a real engineering project development budget. Costs will be mainly divided by their nature in:

- **Direct labour costs**. They correspond to the salary of a junior technical engineer in Spain during the time span of the project. Salary is estimated to be 12 €/h. In order to make an estimation of the working hours, it has been assumed, according to planning B.1, working days of 3h working only Monday to Friday. That summed 194 working days while total worked hours of 582h These costs are displayed below in table B.2.
- **Equipment cost**. These expenses include the amortization cost of the software and hardware, displayed in table B.3.
  - Software. Matlab was used generally for everything in the project, from simulation to results representation. Moreover, Photoshop and Sketchup were used to generate figures and visuals. Lastly, excel office was employed at specific moments. However, the academic version of Matlab and office licenses are provided by the university. For the rest, the author already possessed the corresponding licenses. Thus there is no associated cost of acquiring them.
  - Hardware. A computer was used for this project. A Huawei Matebook D laptop valued at 1000 €with an expected lifespan of 4 years. Linear amortization during the time was applied assuming a use of 8 hours its lifespan.

- **Indirect costs**. It will be included as indirect cost the ones that there is no direct relationship with the work performed. Indirect costs as the internet will not be taken into account following the previous reasoning, as they are already contracted and no additional cost is encountered. Therefore indirect costs are gathered in table B.4.
  - Indirect labour cost. it will include supervisor salary for the working time employed helping on this project. The contribution has been quantified to be around 45h with a salary of 24€/h, which summed 1080 €.
  - Electricity cost. It is quite difficult to quantify since it fluctuates not only monthly but by hours. An average of the day of 0.101 €/kWh is taken since it is not the higher neither the lower. Computer consumes around 0.044KWh by assembler information. Electricity computer consumption over 582 hours of used will be translated in the tiny amount of 3€.

	Working hours	Cost/hour	Total
Direct labour costs	582	12 €/h	6984 €

Table B.2. Direct labour costs

	Initial value	Lifespan	Estimated use	Total depreciation cost
Hauwei Matebook	1000 €	4 years	582 h	49 €

Table B.3. Equipment costs

	Cost
Indirect Labour costs	1080 €
Electricity	3 €
Total	1083 €

Table B.4. Indirect costs

Direct labour costs	6984 €
Equipment cost	49 €
Indirect cost	1083 €
Total	8116 €

Table B.5. Total estimated budget